



# Characterization of shock-induced panel flutter with simultaneous use of DIC and PIV

A. D'Aguanno<sup>1</sup> · P. Quesada Allerhand<sup>1</sup> · F. F. J. Schrijer<sup>1</sup> · B. W. van Oudheusden<sup>1</sup>

Received: 9 July 2022 / Revised: 21 October 2022 / Accepted: 13 December 2022 / Published online: 5 January 2023  
© The Author(s) 2023

## Abstract

In this experimental study, panel flutter induced by an impinging oblique shockwave is investigated at a freestream Mach number of 2, using the combination of planar particle image velocimetry (PIV) and stereographic digital image correlation (DIC) to obtain simultaneous full-field structural displacement and flow velocity measurements. High-speed cameras are employed to obtain a time-resolved description of the panel motion and the shockwave-boundary layer interaction (SWBLI). In order to prevent interference between the PIV and DIC systems, an optical isolation is implemented using fluorescent paint, dedicated light sources, and camera lens filters. The effect of the panel motion on the SWBLI behavior is assessed, by comparing it with the SWBLI on a rigid wall. The results show that panel oscillations occur with a maximum amplitude of ten times the panel thickness. The dominant frequencies observed in the panel oscillation (424 Hz and 1354 Hz) match the main spectral content of the reflected shockwave position. A further POD analysis of the panel displacement spatial distribution shows that these two frequency contributions are well captured by the first two POD modes, which correspond, respectively, to a first and a third bending mode shape and account for 92% of the total oscillation energy. The fluid-structure coupling is studied by identifying, in the flow, the regions of maximum correlation between the panel displacement and the flow velocity fluctuations. The results obtained prove that the inviscid flow region upstream of the SWBLI is perfectly in phase with the panel oscillation, while the downstream region has a delay of one quarter of the flutter cycle.

## 1 Introduction

The vibration of thin structural surface elements exposed to a supersonic flow represents a fluid-structure interaction (FSI) phenomenon that can seriously affect the performance and structural integrity of supersonic aircraft and spacecraft systems. These adverse effects are further amplified when a shockwave/boundary-layer interaction (SWBLI) occurs over the panel, since the increased pressure and thermal loads over the panel further compromise the strength and stiffness of the plate (Spottswood et al. 2019). Panel flutter induced by a SWBLI has been observed for a multitude of high-speed vehicles (Dowell and Bendiksen 2010), such as the X-15 (Watts 1968), in the operation of a non-adaptable exhaust nozzle (like that of a launch vehicle) during the start-up phase (Östlund et al. 2004 and Garelli et al. 2010)

or for single stage to orbit vehicles (Blevins et al. 1993). The accompanying over-expanded flow can lead to shockwave boundary layer interaction on the flexible nozzle wall, where impinging oblique shocks trigger violent oscillations of the nozzle (Pasquariello 2018). The occurrence of panel flutter is undesirable, as it can cause fatigue failure of the excited thin-wall due to prolonged periodic oscillations. A better understanding of this phenomenon, which is generally referred to as shock-induced panel flutter (Boyer et al. 2018), is therefore crucial for the design of future high-speed vehicles.

### 1.1 Shock-induced-fluid structure interaction

For an inviscid flow, when an oblique shockwave impinges on a flat surface, the flow direction immediately downstream of the shockwave changes by the imposed deflection angle. To satisfy the non-permeability condition at the wall, a reflected shockwave originates in the impinging point, to restore the original flow deflection, parallel to the wall.

In a real flow a boundary layer (BL) is developing over the wall, causing the impinging shockwave bends upon

✉ A. D'Aguanno  
A.Daguanno@tudelft.nl

<sup>1</sup> Faculty of Aerospace Engineering, Aerodynamics Section, Delft University of Technology, Kluyverweg 2, 2629HS Delft, The Netherlands

reaching the boundary layer and becomes weaker until it vanishes in correspondence of the sonic line as sketched in Fig. 1 (left). The increase in pressure created by the shock-wave propagates upstream in the subsonic region of the boundary layer. This effect significantly increases the boundary-layer thickness, and may even induce separation well upstream of the shock impingement point. The change in the displacement effect of the boundary layer causes the flow to turn away from the wall at separation and again toward it at reattachment. Thus, additional systems of compression and expansion waves are generated, with the compression system formed upstream of the separated flow coalescing into a shockwave (reflected shockwave). This interaction system has been observed to possess an unsteady character, meaning that the position of the separation bubble and of the reflected shockwave vary in time, usually at a low-frequency, relative to the time scales of the incoming boundary layer. The SWBLI developing on a rigid surface has received extensive attention, and a more detailed description can be found in reference texts, such as given by Babinsky and Harvey (2011).

The origin of the low-frequency unsteadiness of the interaction remains an issue of discussion (Dolling 2001; Shinde et al. 2019) while it is considered to be one of the driving mechanisms for the coupling between fluid and structure in the case of a flexible surface. Because of its relevance, the study of SWBLI is still a topic of interest both in presence of a thin and of a rigid panel.

Supersonic panel flutter has been extensively studied in literature, with Dowell (1975) presenting an overview of the theoretical models and the physical aspects of flutter, while Mei et al. (1999) has given a general review of the most relevant results on panel flutter in the last century. A more recent review is provided by Dowell and Bendiksen (2010), which also gives attention to viscosity effects.

Several numerical studies have approached shock-induced panel flutter in the recent years. One of the earliest studies

is Visbal (2012), where the compressible Euler equations were coupled with the von Karman plate equation for a two-dimensional panel. Inviscid 3D flutter is instead investigated by Boyer et al. (2018) who considered a panel clamped on all edges. Viscosity effects on 2D panels have been taken into account by Visbal (2014) and later by Pasquariello et al. (2015), which used LES to study shock-induced panel flutter with additional unsteadiness imposed by a pitching shock generator; differently Brouwer et al. (2017) has investigated the effects of a compliant surface on the separation bubble dynamics of SWBLI. Viscosity effects for three-dimensional (3D) flutter have been studied by Shinde et al. (2018), which considered flutter induced by a transitional SWBLI.

The use of numerical simulations has the attractive feature (when compared to experiments) of providing complete flow characterization data with a high spatial and temporal resolution, and with the opportunity of conveniently changing the main flow and structural parameters at will. However, numerical simulations are also characterized by important drawbacks, such as the limited Reynolds number and the limited computational domain. High fidelity fluid structure interaction simulations are also limited in describing the relatively large time scales of the structure dynamics. Also, uncertainties in the way the flow and structure are modeled, including the boundary conditions, may affect the extent to which numerical solutions can represent actual technical configurations. Therefore, the comparison and validation of simulations with experimental data has a high value.

## 1.2 Measurement techniques development

In a typical flutter experiment, a flat (or curved) plate is assembled in the wind tunnel test section and the dynamic pressure of the wind tunnel is increased until flutter is achieved. Many experimental studies in the past were focused on determining the effects of different geometry, flow and boundary conditions on the flutter boundaries.

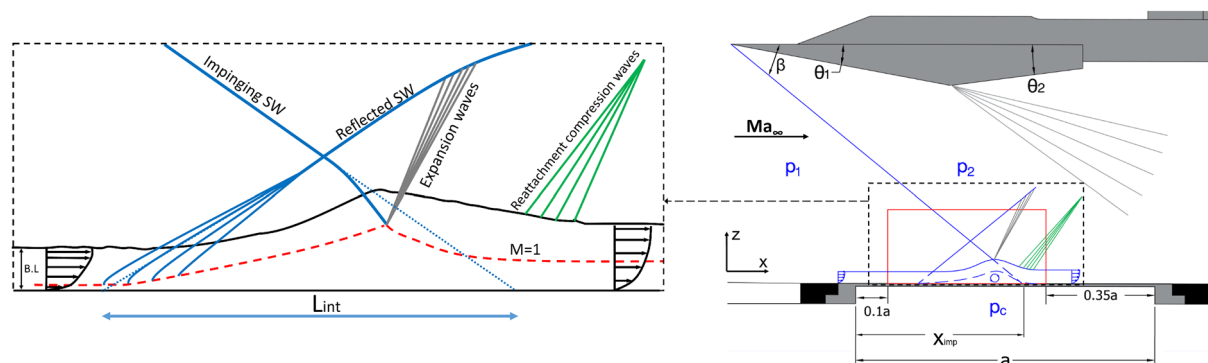


**Fig. 1** Schematic overview of the SWBLI developing on a rigid panel (left). On the right sketch of the experimental geometry, including the PIV FOV outlined in red (side-view)

Anderson (1962) determined the flutter boundaries of flat and curved plates at a Mach number of 2.81 using inductance pickups to measure the plate vibration, while Dowell and Voss (1965) performed various experiments studying the effect of panel dimensions, panel mechanical properties, Mach number, and acoustic cavity size on flutter boundaries. The plate displacement and strain were measured using vibrometers and strain gauges while the temperature of the plate was monitored with thermocouples. In these experiments only a limited characterization of the flow was performed, typically providing only freestream Mach number and dynamic pressure.

Unfortunately, the experimental techniques as used in these previous studies allow only single point measurements of the flow and the plate displacement, whereas computational simulations allow a full-field analysis of both the plate motion and the surrounding flow. To provide complimentary full flow-field experimental data, more advanced measurement techniques, such as particle image velocimetry (PIV), should be incorporated. Very few experimental studies using full flow-field techniques have been used to investigate shock induced panel flutter. On the other hand, these techniques have already been extensively used under similar conditions for the study of a shockwave impinging on a rigid plate as documented in the review paper of Clemens and Narayanaswamy (2014). A qualitative description of the full flow-field can be achieved with schlieren visualization, which has been employed by Dupont et al. (2006) to investigate the space and time organization of a SWBLI. One of the first applications of PIV to SWBLI is given by Beresh et al. (1998) which studied SWBLI induced by a compression ramp. For a similar application, Ganapathisubramani et al. (2009) has investigated with high-speed PIV (6kHz) the origin of the low frequency unsteadiness of the separated area, and attributed them to “global” and “local” influences of the incoming boundary layer. Differently, SWBLI induced by an impinging shockwave is described by Humble et al. (2007) using planar PIV. In a following study van Oudheusden et al. (2011) used high-speed PIV to measure the time-resolved 2D flow of a SWBLI and to study the associated flow unsteadiness. Piponniau et al. (2009) has used PIV data to verify a model which explains the low-frequency unsteadiness for cases in which the flow is reattaching downstream of the impinging shockwave. Furthermore, Schreyer et al. (2015) studied SWBLI using a dual PIV system (multi-exposure) to simultaneously achieve a sufficiently high spatial and temporal resolution. A dual-PIV investigation is also carried out by Souverein et al. (2009), where the laser lights of the two PIV systems were optically distinguished by means of polarization. By using tomographic PIV, Humble et al. (2009) have analyzed the instantaneous 3D flow structure of a SWBLI, showing the presence of hairpin-type vortical structures, which are associated with low-momentum regions.

Regarding the experimental characterization of the shock-induced panel flutter itself, Spottswood et al. (2012) used high-speed digital image correlation (DIC) to achieve a detailed measurement of the vibration response of a thin plate during shock-induced panel flutter. The use of DIC provided a complete description of the plate displacement, which allowed the extraction of the panel vibration mode shapes. Pressure sensitive paint (PSP) was used to quantify the pressure distribution on the plate surface even if no accompanying flow field measurements were performed. Further panel flutter investigation employing PSP measurements have also been conducted by Neet and Austin (2020) and Tripathi et al. (2021). Spottswood et al. (2019) employed DIC to record the panel movement from both the cavity and the flow side, to quantify the effect of optical aberration effects, without noticing relevant differences. The suitability of DIC for the study of supersonic panel flutter (although in absence of shockwave impingement), was also confirmed by D’Aguanno et al. (2019), where DIC measurements showed excellent agreement with reliable pointwise laser vibrometer measurements. Recently, Brouwer et al. (2021) conducted full field DIC measurements of a thermally buckled panel, and similarly Daub et al. (2020) successfully applied DIC to a hypersonic fluid-structure interaction in presence of high thermal loads and plastic deformation. An analogous flow application was investigated by Whalen et al. (2020) using a similar experimental technique: photogrammetry.

The experimental data have also confirmed that the boundary condition plays a significant role on the dynamics of the interaction in terms of flutter boundaries, mode shapes and dominant frequencies. These differences are confirmed by the comparison of the performance of panels clamped on all sides (Spottswood et al. 2012; Bebernis et al. 2011) and panels with free side edges (Daub et al. 2016a). However, there is no study which directly investigates the effect of boundary conditions on shock induced panel flutter, unlike regular panel flutter (see Dowell and Bendiksen 2010).

Regarding the analysis of the flow field, the use of shadowgraphy (Tripathi et al. 2021) and schlieren techniques (Daub et al. 2016a; Willems et al. 2013) is already widespread. Although these techniques provide a span-averaged impression of the wave pattern, they do not allow to quantitatively investigate the flow field or to analyze the 3D structures developing over the panel. For this, PIV would be a suitable diagnostic tool to be applied in the study of shock induced panel flutter; however, PIV has been employed in this application only by Tripathi et al. (2021).

### 1.3 Objective

The objective of the current study is to experimentally investigate shock induced panel flutter using PIV and DIC simultaneously, with the aim of assessing the feasibility of using

these selected techniques for this particular fluid-structure interaction, and generating reliable full-field experimental data. To the best of the authors' knowledge no experimental studies on shock induced panel flutter have been reported so far, which employ both DIC and PIV in combination. In contrast, the measurement of both flow and structure using PIV and DIC simultaneously has been documented for low speed fluid-structure interactions, as in Zhang and Porfiri (2019)), which proves the feasibility of the simultaneous use of these techniques. Hortensius et al. (2018) and Ahn et al. (2022) are the only other studies in which these techniques have been used under supersonic flow conditions. In the former study, the interaction between an underexpanded jet and an adjacent compliant surface is investigated without time resolving neither the flow nor the structure, in the latter, the oscillation of a compliant panel under a compression ramp is analyzed.

Although the numerical study of a panel clamped on all sides (making the interaction inherently 3D) has also been carried out in recent years, (see Shinde et al. 2019 and Boyer et al. 2021), most of the existing numerical researches consider quasi-2D interactions with panels that have free edges at the lateral sides (as in Pasquariello et al. (2015) and Visbal (2012)). Therefore, in this study a panel with free side edges has been investigated, predicting a nominally 2D character from both the flow (at least close to the panel centerline; see Bermejo-Moreno et al. (2014) for an analysis of confinement effects) and structural perspective.

## 2 Experimental procedures

### 2.1 ST-15 wind tunnel

The tests have been performed in the ST-15 supersonic blow-down wind tunnel of TU Delft. The tunnel is equipped with interchangeable nozzle blocks, that are mounted on the top and on the bottom wall. For this study the  $Ma = 2$  nozzle was used. The rectangular test section has a size of  $15\text{cm} \times 15\text{cm} \times 25\text{cm}$  with two side windows (diameter of 250 mm) to allow optical access to the test section.

The wind tunnel was operated at a total pressure  $p_0 = 250 \pm 2$  kPa and total temperature  $T_0 = 285 \pm 3$  K. For these stagnation conditions and a free stream Mach number  $Ma_\infty = 2.00 \pm 0.01$ , the corresponding dynamic pressure is  $q_\infty = 88$  kPa. The boundary layer thickness at the entry of the test section is  $\delta_{99,0} = 5.2$  mm (see Giepmans et al. (2018)). The main operational parameters are summarized in Table 1.

### 2.2 Panels

In this study measurements were conducted on both a flexible thin panel and on a rigid plate, with the latter used as a baseline reference case.

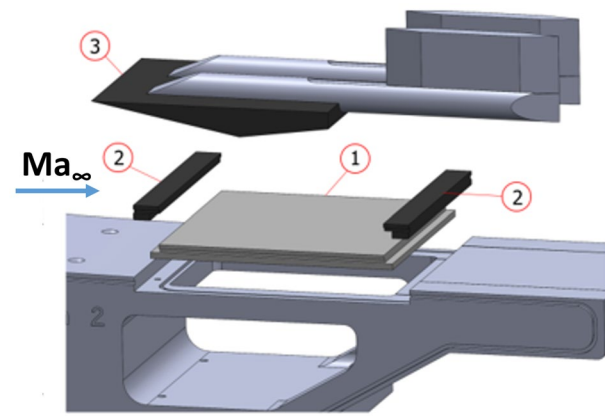


**Fig. 2** 3D CAD rendering of the test section with panel (1), clamping pieces (2) and shock generator (3)

**Table 1** Flow conditions

Parameter	Symbol	Value	Unit
Free stream Mach number	$Ma_\infty$	2.0	
Free stream velocity	$U_\infty$	504	m/s
Total pressure	$p_0$	250	kPa
Total temperature	$T_0$	285	K
Dynamic pressure	$q_\infty$	88	kPa
Boundary layer thickness	$\delta_{99,0}$	5.2	mm
Incompressible momentum thickness	$\theta_i$	0.52	mm
Reynolds number per unit length	$Re_\infty/L$	$32.5 \cdot 10^6$	1/m
Reynolds based on $\theta_i$	$Re_{\theta_i}$	$16.9 \cdot 10^3$	–

All panels were made from Al7075-T6 and installed in the lower Mach block by means of two L-shaped clamping pieces, see Fig. 2. The figure also shows the presence of the cavity underneath the panels, which is directly connected to the exit of the test section. As such the pressure in the cavity during the experiments was not explicitly controlled.

The thin panel has a thickness  $h = 0.3$  mm, length  $a = 128$  mm and a span  $b = 84$  mm, resulting in an aspect ratio  $a/b = 1.5$ . The panel is clamped at the leading and trailing edges while it is free on its sides as shown in Fig. 3 (left). This clamping condition is achieved with two stream-wise oriented cuts of 0.2 mm of width. As the rigid baseline case a 9 mm thick panel was used without side slits (see Fig. 3, right). To give a first estimate of the first natural frequencies of the flexible panel, the finite element software ABAQUS was used. From this analysis the first and second bending modes are observed to occur at, respectively, 112 Hz and 310 Hz.

A shock generator imposing a flow deflection angle of  $\theta_1 = 11^\circ$  was mounted to create an oblique shockwave impinging at  $x_{imp}/a = 0.55$  on the panel. To limit the height of the shock generator, and hence the blockage, the shock

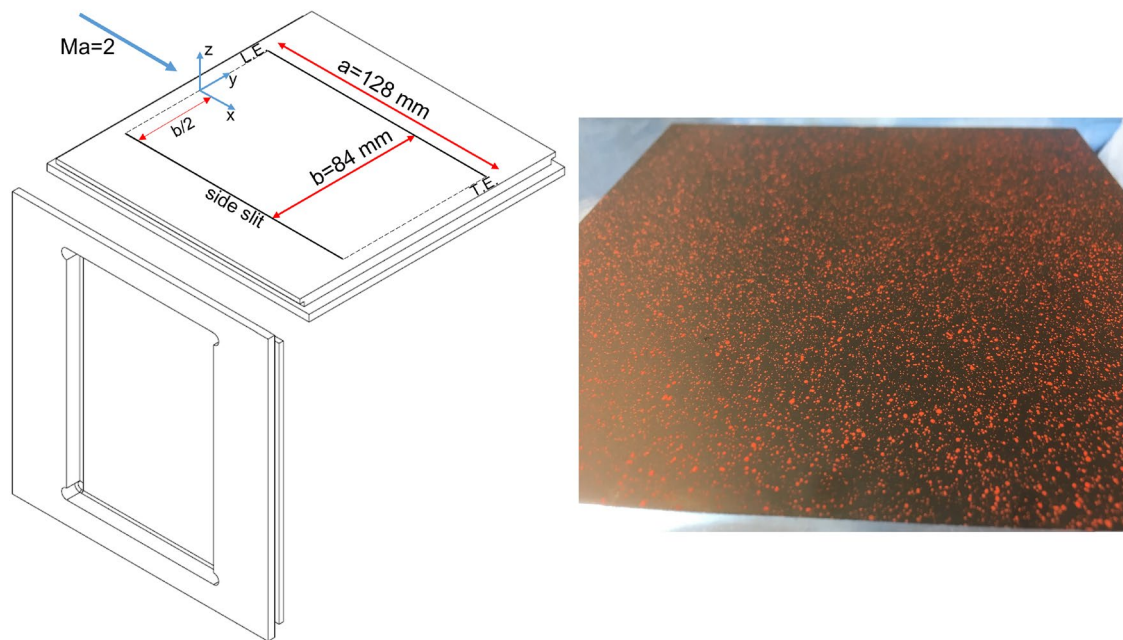


**Fig. 3** Technical drawing of flexible panel (left). On the right, rigid panel with speckle pattern on it

**Table 2** Model parameters

Parameter	Symbol	Value	Unit
Length panel	$a$	128	mm
Span panel	$b$	84	mm
Thickness panels	$h$	0.3	mm
Angle shock generator	$\theta_1$	11	$^\circ$
Second ramp angle	$\theta_2$	7.8	$^\circ$
Impinging shock angle	$\beta$	40.4	$^\circ$
SW impinging point	$x_{imp}/a$	0.55	–
Pressure ratio across impinging SW	$p_2/p_1$	1.8	–

generator has an upward slope of  $\theta_2 = 7.8^\circ$  in the rear. This causes an expansion wave, which impinges on the bottom wall of the test section, downstream of the flexible panel (see Fig. 1, right). In Table 2, the most important panel and shock generator parameters are summarized.

### 2.3 Measurement techniques

The panel deformation is measured by means of DIC, for this two Photron FASTCAM SA1 high speed cameras have been used in a stereographic configuration. The cameras have been placed on one side of the wind tunnel as is shown in Fig. 4 (left). The angle between both cameras is approximately  $45^\circ$ , which is the optimum value to measure out-of-plane displacements (see Sutton et al. 2009). The orientation of the cameras with respect to the measurement plane

is shown in Fig. 4 (right) with the 2 DIC cameras having a symmetrical position with respect to the vertical plane passing through  $x/a=0.5$ . Both cameras were operated at an acquisition frequency of  $5000\text{ Hz}$  and full resolution of  $1024 \times 1024\text{ px}$ . The acquisition frequency has been selected in order to obtain time resolved measurements with respect to the most energetic panel flutter frequencies. Each camera was equipped with a 105 mm Nikkor objective with  $f_\# = 11$  and Scheimpflug adapter to align the focal plane of the cameras with the non-deformed surface of the panel. The resulting depth of focus was approximately 16 mm which was sufficient to keep the deformed plate in focus during the measurements. The resulting DIC FOV is approximately 120 mm long and 100 mm wide, thus including the entire panel (except for small regions at the LE and TE of the panel).

The DIC cameras capture the movement of the panel by tracking a speckle pattern on the surface of the panel. The pattern consisted of air brushed dots of fluorescent paint with a size ranging from 3 to 7 pixels. In order to have a good contrast between the black background and the fluorescent paint, a speckle coverage of nearly 50% of the panel surface was used (see Fig. 3, right). In order to acquire images of the speckle pattern a blue LED lamp was installed between the cameras (see Fig. 4). The LED was synchronized with the DIC cameras by means of a high speed controller with a pulse time  $\tau_{LED} = 20\ \mu\text{s}$ . The synchronization is described in more details in Section 2.4.

The flow field in the center streamwise plane was measured by means of two-component particle image velocimetry. A single camera in planar configuration was employed,

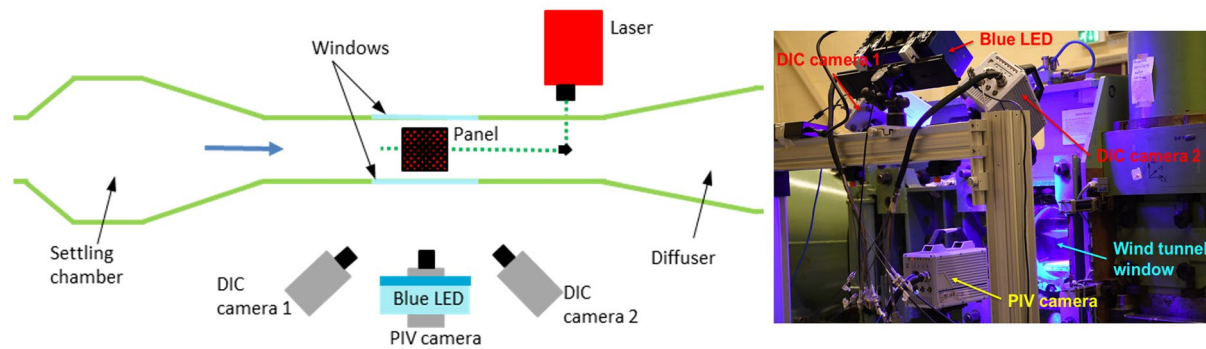


**Fig. 4** On the left sketch of optical measurement set-up (top-view), while on the right picture of the set-up showing the cameras arrangement

acquiring images in a chordwise-vertical oriented plane of measurement passing along the mid-span of the panel, as shown in Figs. 1 (right) and 4. Since the PIV and DIC systems are synchronized, the acquisition frequency was 5000 Hz for the PIV measurements as well. In total, 4719 image pairs were acquired in double pulse mode with an interframe time of  $dt = 2\mu\text{s}$ . The camera was fitted with a lens having a focal length of 105mm with  $f_{\#} = 4$ . These settings were combined with a cropped sensor resolution of  $1024 \times 592\text{px}$  with the PIV FOV extending in streamwise direction from  $x/a = 0.1$  to  $x/a = 0.65$ , and wall normal from  $z/a = 0$  to  $z/a = 0.25$  (see Fig. 1, right). This FOV was selected such as to include the main flow features of the shockwave boundary layer interaction. The cartesian coordinates system which has been used in this study is defined in Fig. 3 (left), with the origin in correspondence of the leading edge of the panel at its centerline spanwise location.

DEHS particles were used as flow tracers, which have a relaxation time  $\tau_p = 2\mu\text{s}$  and a particle diameter  $d_p \approx 1\mu\text{m}$  (see Ragni et al. 2011 for more details). The seeding particles were illuminated by Nd:YAG Continuum MESA PIV dual cavity laser. The 1 mm thick light sheet was formed and introduced into the test section by means of a periscope probe.

To assess the presence of wind-tunnel vibrations, an accelerometer was mounted on the lower Mach block, showing the presence of facility vibrations at 576 Hz.

## 2.4 Synchronization and optical separation

A LaVision high-speed controller was used to synchronize the laser and PIV camera, the same trigger pulses were also used to control the DIC cameras. The trigger of the second laser pulse in combination with a Stanford GD535 digital delay/pulse generator was used to control the pulse duration of the LED light source. Because the PIV and DIC measurements are performed simultaneously, it was necessary to optically separate both systems.

An orange fluorescent water based paint from LaVision (article number 1012056) has been selected for the speckle pattern so that when it is illuminated by the blue LED ( $\lambda_{LED} \sim 420 - 500\text{nm}$ ), the fluorescent emission of the paint occurs at higher wavelengths than the laser ( $\lambda_{Paint} \sim 600 - 750\text{nm}$ , while  $\lambda_{Laser} = 532\text{nm}$ ). To ensure that the DIC acquisition is not affected by the PIV illumination system and vice versa, appropriate optical filters were fitted on all camera lenses. For the DIC cameras, highpass filters have been employed with a cut-off wavelength  $\lambda_{HP} = 580\text{nm}$ , to avoid any illumination from the laser. Similarly on the PIV camera a bandpass filter ( $\lambda_{BP} \sim 475 - 575\text{nm}$ ) has been used to avoid illumination from both the blue LED and the fluorescent paint.

Figure 5 indicates the emission wavelength spectra of the light sources and of the fluorescent paint and the transmitted wavelength spectra of the camera optical filters.

The effect of using the highpass filters is demonstrated in Fig. 6, which shows the raw DIC images acquired both without (Fig. 6-left) and with (Fig. 6-center) filters. Both images have been acquired in presence of PIV seeding that is illuminated by the PIV laser. In the image on the left, the presence of the laser sheet, makes the evaluation of the panel displacement field near the mid-span less reliable due to the increase background light. The use of the DIC camera filter (center image) prevents this effect, with only a small contribution of laser reflections on the surface still visible. To quantify this aspect, a histogram of the pixel intensity is shown for the blue and orange  $50 \times 50$  pix square regions shown in Fig. 6. The histogram for the image without DIC filter, reveals that due to the laser illumination, all pixel intensity values are above 200 counts. In contrast, with the highpass filter applied, a better contrast is achieved between the black background and the intensity counts of the speckle pattern.

Also for the PIV bandpass filter, the histograms of the pixel intensity were determined (see Fig. 7) for the two configurations (with and without filter) in two square regions of

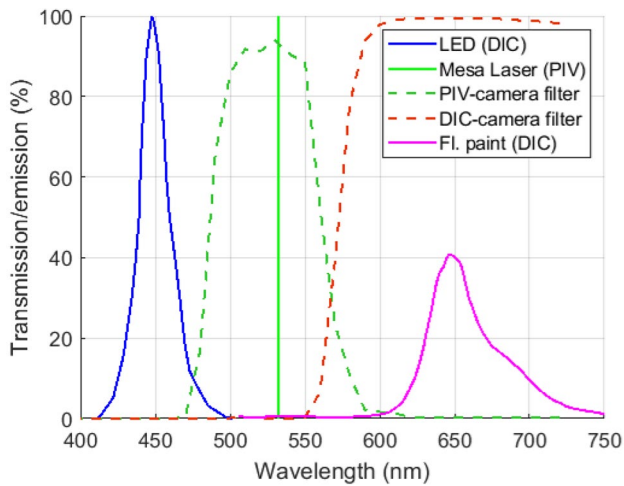


**Fig. 5** Transmission/emission spectra used for optical separation of the PIV/DIC systems

$50 \times 50px$  each. The corresponding distributions reveal that the effect of the filter is that of shifting the entire distribution to lower counts of pixel intensity.

However, although the bandpass filter helps to minimize the reflections on the wall of the panel due to the LED, it was

found that it has only a marginal effect on the evaluation of the velocity vectors. This observation is associated with the fact that, even without the PIV filter, the DIC light is not able to sufficiently illuminate the seeding particles.

### 2.5 Data processing

As it is clear from Fig. 7, the raw PIV snapshots suffer from significant laser light reflections from the surface of the panel. Therefore the images were pre-processed by means of a Butterworth time filter having a length of seven images (Sciacchitano and Scarano 2014). In addition, the region in which the panel was oscillating was completely masked to avoid outliers in proximity of the surface of the panel. Thus the vertical extent of the field of view in which velocity vectors are obtained is limited from  $z/a = 0.032$  to  $z/a = 0.25$  (the latter being the original upper boundary of the FOV, see Section 2.3). The velocity vectors were subsequently obtained from a multi-pass cross-correlation analysis with a window size of  $96 \times 96px$  and three additional passes with a circular window size of  $24 \times 24px$ . The overlap was set to 75% which results in a final vector spacing of  $\Delta x_{PIV} = 0.38mm$  corresponding to  $\Delta x_{PIV}/a = 0.003$ .

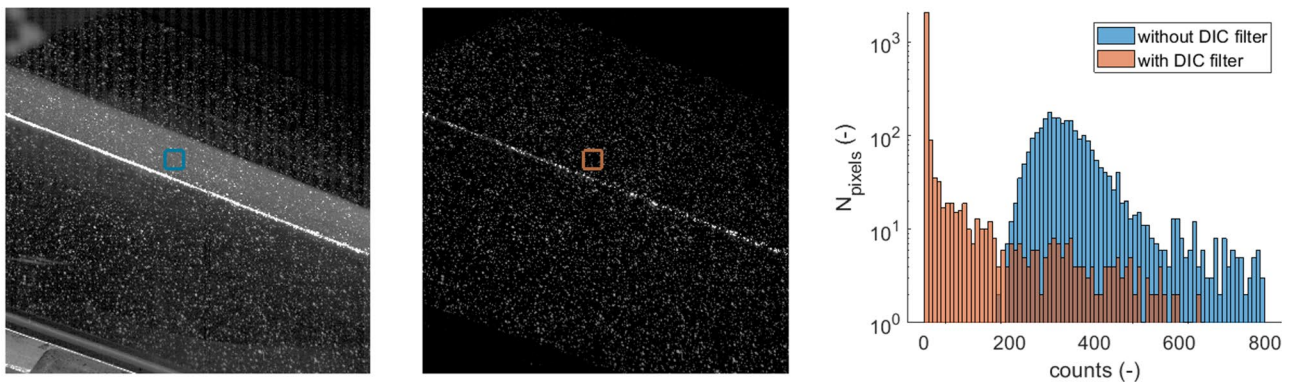


**Fig. 6** Comparison of DIC raw images without (left) and with (right) highpass filter. On the right an histogram shows the image counts distribution for two square regions (blue on the left image and orange in the center) belonging to the two DIC raw images

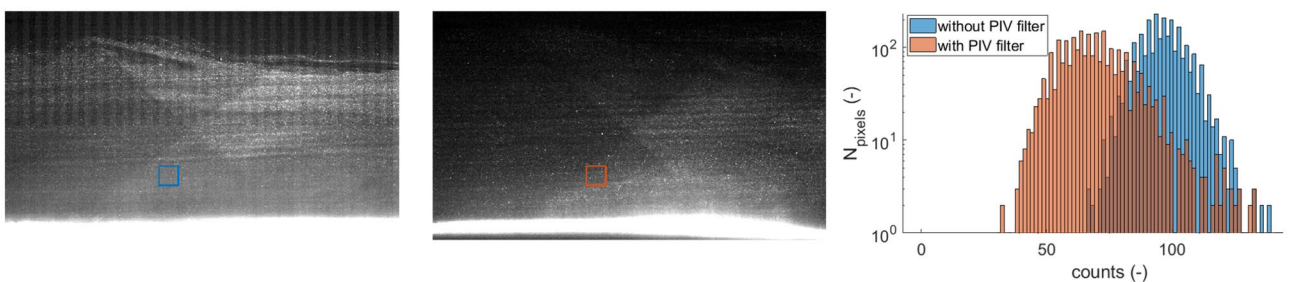


**Fig. 7** Comparison of PIV raw images without (left) and with (right) bandpass filter. On the right the histogram shows the image counts distribution for the indicated two square regions (blue on the left image and orange in the center)

For the DIC data, the displacement field has been evaluated with a cross-correlation procedure, in which each instantaneous raw image is correlated with a reference image, that is the average of 100 images in absence of flow (static panel position). A window (subset) size of  $39 \times 39$  pixels with an overlap of 66% has been used, which results in a vector spacing of  $\Delta x_{DIC}/a = 0.011$ . The cross-correlation is limited to estimate only the translational displacement of the speckle pattern in the interrogation window. However, the 3D deformation of the panel could cause the subset pair of one image to differ greatly from the reference image. To minimize these differences a least squares matching method is used to map the intensity field of the reference image into coordinates of the instantaneous raw image of the deforming panel.

A summary of the main DIC and PIV settings is reported in Table 3.

All the data acquisition, pre-processing and cross-correlation of the acquired images have been performed in Davis 10.1 from LaVision. Additional post-processing has been performed in Matlab.

## 2.6 Uncertainty analysis

The main sources of uncertainty for both the DIC and PIV techniques are discussed below, with the estimated values collected in Table 4.

For the PIV data the highest source of uncertainty on the velocity value is the uncertainty caused by the particle slip. This uncertainty is caused by the effect that the tracer particles do not perfectly follow the flow in presence of accelerations induced by large pressure gradients (as notably introduced by shockwaves). This slip can be quantified in terms of the particle relaxation time, which, as previously mentioned is  $\tau_p = 2 \mu\text{s}$ . The magnitude of this uncertainty is very significant in the region directly downstream of a shockwave ( $\epsilon_{slip} < 53.36 \text{ m/s}$ ); however, it can be considered negligible in the remaining FOV. The particle slip has a non-negligible consequence in tracking the reflected shockwave position in all the instantaneous PIV images. Considering the value of  $\tau_p$ , the corresponding relaxation length ( $\zeta_p$ ) can be derived, obtaining a value

**Table 4** Uncertainty errors

Uncertainty source	Technique	Value	Unit
Statistical $\epsilon_u$	PIV	< 0.25	<i>m/s</i>
Statistical $\epsilon_v$	PIV	< 0.21	<i>m/s</i>
Global uncertainty on displacement field $\epsilon_z$	DIC	< 0.02	<i>mm</i>
Cross-correlation $\epsilon_{cc}$	PIV	< 3.42	<i>m/s</i>
Particle slip $\epsilon_{slip}$	PIV	< 53.36	<i>m/s</i>
Shockwave tracking $\epsilon_{SW}$	PIV	< 0.24	<i>mm</i>
Spatial resolution (interrogation window size)	PIV	< 1.67	<i>mm</i>
Spatial resolution (subset size)	DIC	< 4.57	<i>mm</i>

of  $\zeta_p = 0.64 \text{ mm}$  (see Ragni et al. (2011) for more details). The uncertainty in tracking the reflected shockwave ( $\epsilon_{SW}$ ) can be estimated as half of the relaxation length value projected in the horizontal direction, thus equal to 0.24 mm (or 0.19%a).

To verify the accuracy of the experimental procedure, the statistical uncertainty is also computed in regions of the flow where virtually no fluctuations are expected. Therefore, this uncertainty is computed for the PIV measurements in the supersonic free stream region upstream of the impinging shockwave, yielding values of  $\epsilon_u < 0.25 \text{ m/s}$  and  $\epsilon_v < 0.21 \text{ m/s}$ , respectively, for the horizontal and vertical component. Also, the cross correlation procedure used in PIV, brings an uncertainty estimated as  $\epsilon_{cc} < 3.42 \text{ m/s}$  (see Humble (2009) for its computation).

The uncertainty on the displacement field depends on several aspects, among others: the accuracy of the DIC procedure, wind tunnel vibrations, and optical aberration effects. Aberration effects for DIC measurements have been investigated by Spottswood et al. (2019) and Beberniss and Ehrhardt (2021) and considered to be non-significant and of the same order of magnitude as other sources of uncertainty. To globally quantify the uncertainty associated with all these aspects, DIC measurements were carried out on the rigid plate in presence of shockwave impingement. The overall uncertainty of the measurement procedure can be conservatively computed as the

**Table 3** DIC and PIV settings

Setting	DIC	PIV
Acquisition frequency	5 kHz	5 kHz
Number of images	4719	4719 (pairs)
Final resolution	1024 × 1024 pix	1024 × 592 pix
Field of view (x/a)	0.04–0.98	0.10 - 0.65
Vector spacing ( $\Delta x$ )	1.40 mm (0.011 a)	0.38 mm (0.003 a)
Final window size	39 × 39 pix (4.22 × 4.22 mm)	24 × 24 pix (1.54 × 1.54 mm)
Window overlap	66%	75%



highest value of standard deviation in the displacement field. Accordingly, the global uncertainty on the displacement field is quantified as  $\epsilon_z < 0.02 \text{ mm}$ .

### 3 Results

#### 3.1 Instantaneous behavior

A first sequence of the shock-induced fluid structure interaction taking place over the flexible thin panel with shock impingement at  $0.55a$  is shown in Fig. 8, where the instantaneous horizontal velocity field is shown together with the vertical displacement field of the panel for different stages of a flutter cycle. The figure illustrates the capability of the set-up to capture the dynamics of both the flow field and the structural deformation. The flutter cycle is shown in Fig. 8, where four snapshots with a fixed temporal spacing of  $0.6 \text{ ms}$  are shown. The snapshots reveal that the panel is oscillating between a most upward (experienced in the first time step with maximum value of  $z/h \approx 6$ ) and a most downward deformation (which is observable for  $t = t_0 + 1.2 \text{ ms}$ , with  $z/h \approx -6$ ). In the two intermediate stages ( $t = t_0 + 0.6 \text{ ms}$  and  $t = t_0 + 1.8 \text{ ms}$ ) the panel deformation is smaller and shows a combination of upward and downward deflection along the plate. Near the leading edge the panel has always a positive (upward) deformation, while it is negative near the trailing edge, which suggests the presence of a nonzero mean deformation. Together with the panel motion, the main flow features, as sketched in Fig. 1 (left) are also observed in the measured velocity fields, namely the impinging shock-wave, the separated area induced by the shock impingement (green-blue area), the resulting reflected shockwave and the expansion. The reflected shock is clearly unsteady and oscillating with the panel motion, being in its most downstream position ( $x/a \approx 0.3$ ) for  $t = t_0 + 0.6 \text{ ms}$  and most upstream

( $x/a \approx 0.2$ ) for  $t = t_0 + 1.8 \text{ ms}$ . In addition to the classical SWBLI flow structures, an oblique compression wave emanating from the leading edge of the panel occurs on account of the steady positive displacement of the panel at this location. In the region included between the leading edge compression wave and the reflected shockwave, additional pressure waves are present. In view of the variation in shape of the panel, the intensity of these waves changes throughout the flutter cycle, with the stronger compression waves being present in Phase 1, for which the panel experiences the most positive deformation.

#### 3.2 Main statistics

In Fig. 9 the average and standard deviation of the vertical displacement fields of the flexible panel are shown. The average displacement (Fig. 9, left) is not zero, as was already qualitatively inferred from Fig. 8. The profile of the average displacement field along the streamwise direction has a sinusoidal shape (second bending mode) which is induced by the distribution of the average pressure difference between the upper and lower side of the panel. The pressure on the upper surface of the panel increases when moving downstream through the interaction region while the pressure in the cavity is expected to be constant. This deformation shape was also reported by Visbal (2014) and Shinde et al. (2019b), but differs from the displacement reported by Willems et al. (2013), where a typical first bending mode shape (with downward deflection) was reported for the average deflection of the panel. This behavior may be associated with a difference in the cavity pressure.

The strength of the panel oscillation is characterized by the standard deviation of the panel displacement as shown in Fig. 9 (right). The distribution is approximately symmetric with respect to the mid-panel location  $x/a = 0.5$ , having the

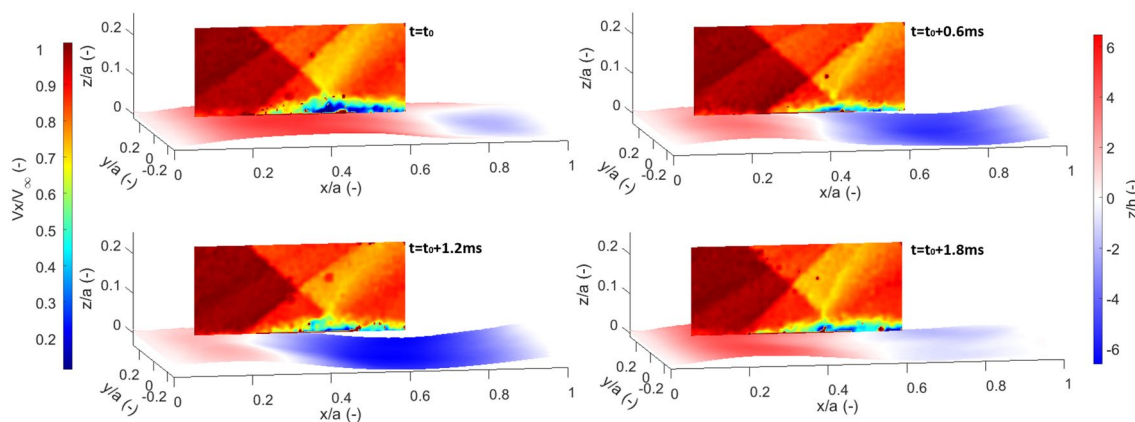


**Fig. 8** Simultaneous velocity and displacement field snapshots for a full flutter cycle

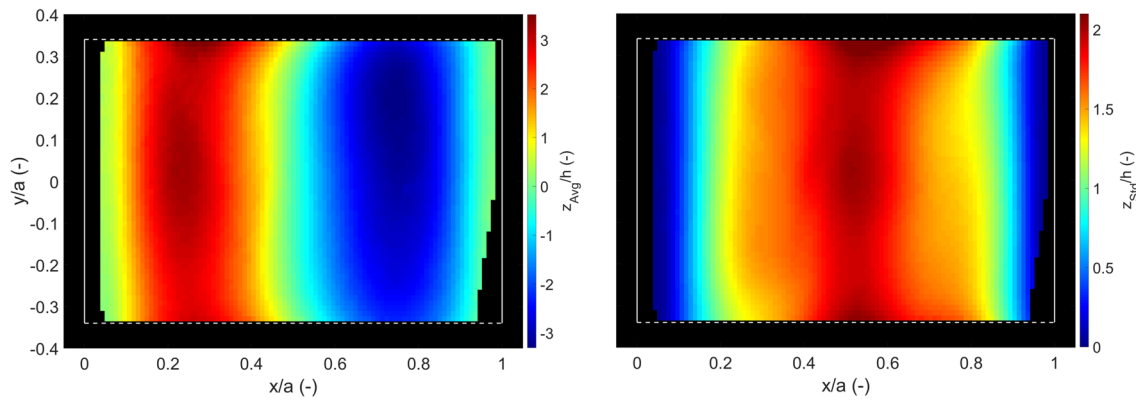


**Fig. 9** Average (left) and standard deviation (right) of the displacement of the panel

highest values in the center of the panel ( $z_{Std}/h = 2$ ) which decreases toward the leading and trailing edge.

Both the average and the standard deviation are very coherent along the spanwise direction, showing that the plate oscillation is predominantly two-dimensional.

In comparison the average and the standard deviation of the horizontal and vertical velocity fields are shown in Figs. 10 and 11 for both the flexible and the rigid panel. As previously commented, the near wall region for  $z/a < 0.032$  is obscured by laser reflections and panel oscillation, for consistency this region has also been masked for the rigid plate. From the average velocity distributions (Fig. 10), the shockwave structures are clearly visible. Furthermore, the vertical velocity data (Fig. 10, right) confirm an upward deflection of the outer flow field for  $0.25 < x/a < 0.45$

in correspondence to the separated area and a downward deflection of the flow for  $x/a > 0.45$ .

When comparing the compliant to the rigid panel, a compression wave appears at the leading edge of the former (as also observed in the instantaneous images, see Fig. 8). As a result of compression waves in the front of the panel, a reduction in the streamwise velocity component and an increase in the vertical velocity component (the flow is deflected upwards) occurs. Another difference between the behavior of the two panels is associated with the occurrence of the expansion waves downstream of the impinging shock-wave, which appear slightly more intense in the rigid panel case. This aspect is thought to be associated with a reduced fluctuation of these waves for the rigid panel, which as a result appear less smeared out.

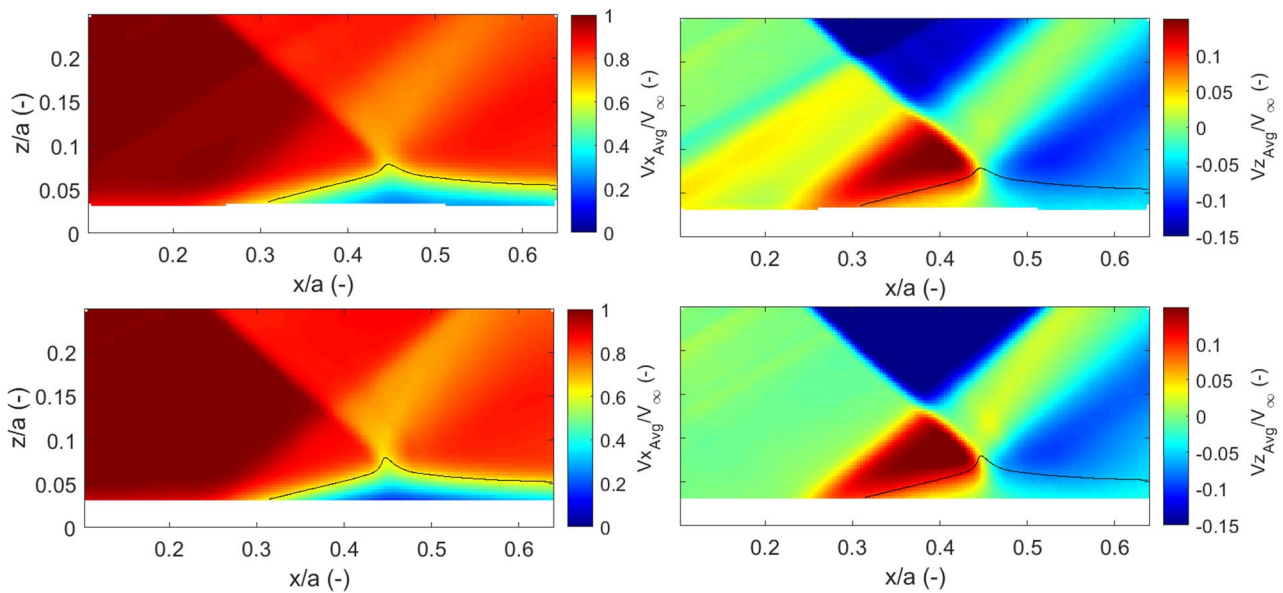


**Fig. 10** Average horizontal (left) and vertical (right) velocity fields for flexible (top) and rigid panel (bottom) with sonic line indicated in black

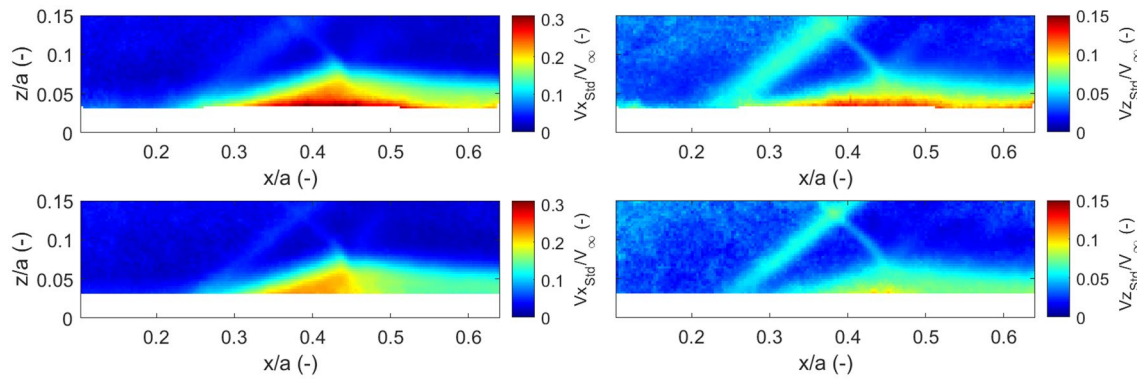


**Fig. 11** Standard deviation of horizontal (left) and vertical velocity component (right) for flexible (top) and rigid panel (bottom)

The standard deviation of the velocity components, for both the panels, highlights that the regions of higher unsteadiness are associated with the separated area and the reflected shockwave. It is interesting to note that no increased values of the standard deviation are observed for the impinging shock or with the compression wave emanating from the leading edge of the panel. This second observation confirms that, at that location, the panel is always bent upwards (as the average and standard deviation of the displacement suggests).

When comparing the behavior of both panels, it is clear that for the flexible panel, the reflected shockwave oscillation range is extended and the fluctuations in the separated area more intense.

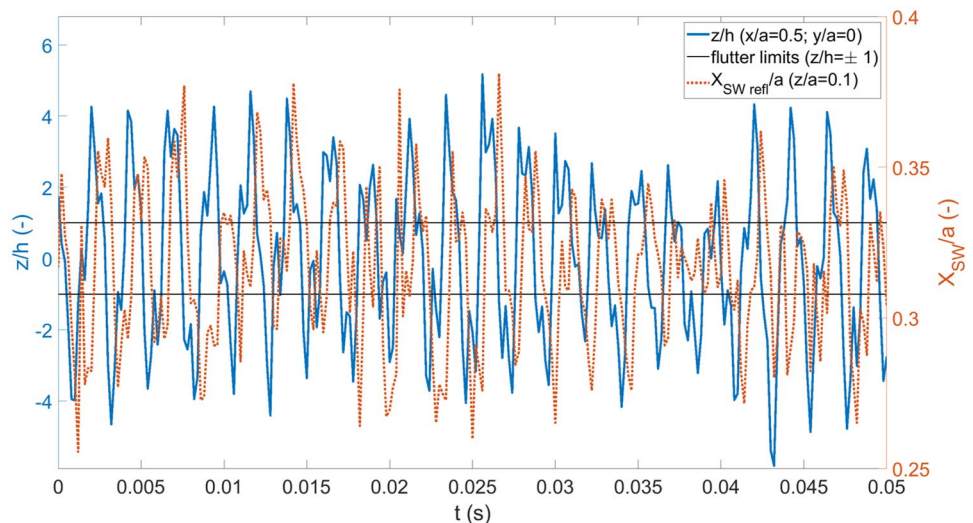
To further analyze the behavior of the flow and structure, the temporal variation of the displacement at one point of the panel is compared to that of the reflected shockwave position (see Fig. 12). The panel displacement is evaluated at the center of the panel ( $x/a = 0.5$  and  $y/a = 0$ ) which has the largest standard deviation. The reflected shockwave

position has been tracked by determining the minimum of the velocity divergence along a horizontal line taken at vertical distance  $z/a = 0.1$ .

The oscillation range of the panel ( $-5 < z/h < 5$ ) is well above the value of the thickness of the panel ( $z/h = \pm 1$ ), which is often referred to in literature as the threshold for the definition of the occurrence of supersonic panel flutter (see Dowell 1970). It is also evident that, although the signal appears as quasi-periodic, the amplitude of oscillation is not constant in time. A similar behavior has been mentioned in both numerical (Visbal 2014; Shinde et al. 2019b) and experimental studies (Beberriss et al. 2016; Spottswood et al. 2019).

On the other hand, the shockwave is oscillating in the range  $0.26 < x/a < 0.38$  ( $\Delta X_{SWrefl} \approx 0.12a = 2.95\delta_{99,0}$ ), with variations in amplitude consistent with the simultaneous behavior of the amplitude of oscillation of the panel. Thus, a good agreement between the two signals is observed (Fig. 12), although the shockwave signal ( $X_{SWrefl}/a$ ) appears to have a lag with respect to the structure oscillation ( $z/h$ ).

**Fig. 12** Temporal behavior of the displacement of the panel (in  $x/a=0.5$ ;  $y/a=0$ ) and of the reflected shockwave position



This confirms that the fluctuations of the flow and the structure fields are strongly correlated.

### 3.3 Spectral analysis

Figure 13 shows a spectral analysis of the reflected shockwave position (red curve) and the flexible panel displacement (blue curve) signals (as displayed in Fig. 12) in the form of the pre-multiplied power spectral density (PSD). To directly compare the two spectra, both PSDs have been normalized by the variance of the respective time signal.

The plot shows a very similar spectral content, with both signals exhibiting a main spectral content around 424 Hz, a secondary peak at 1354 Hz and a tertiary contribution at 576 Hz. The presence of these multiple spectral contributions can be connected to the temporal oscillation shown in Fig. 12, where a lower and a higher frequency contribution are observed. As anticipated in Section 2.3 the peak at 576 Hz is associated with a wind tunnel vibration contribution, while the remaining two peaks with the flutter phenomenon.

For comparison, the premultiplied PSD of the reflected shockwave in presence of the rigid panel is also included in the same figure, normalized once again by the respective

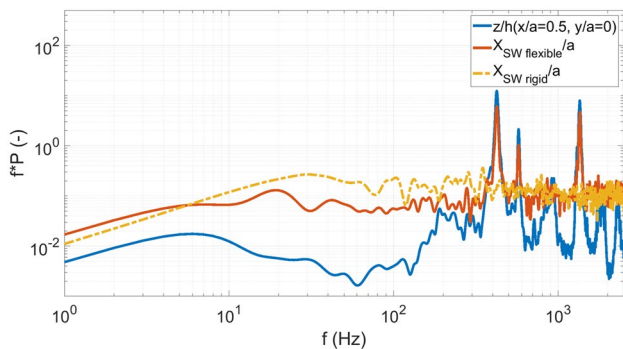


Fig. 13 PSD of reflected shockwave position and panel displacement

variance (see values of standard deviation in Table 5). Compared to the flexible panel, it is clear that for the rigid panel, the oscillation of the reflected shockwave is much less energetic and the spectrum distribution almost flat (with marginally higher contributions for  $200 < f < 350$  Hz).

Spectrograms in the streamwise and spanwise direction were used to verify whether the spectral content of the displacement field is changing over the panel (Fig. 14). The spectrogram along the centerline ( $y/a = 0$ ) of the panel (see Fig. 14, left) shows that the relevance of the three main frequency contributions identified in Fig. 13 (424, 576, 1354 Hz) varies along the chord of the panel. At the center of the panel the dominant contribution is at 424 Hz, while toward the leading and trailing edge is at 1354 Hz (with the wind tunnel contribution at 576 Hz being almost completely absent close to the clamped sides of the panel). The strength of the spectral peak at 1354 Hz appears to be zero at 1/3 and 2/3 of the length of the panel, suggesting that the spatial distribution associated with this mode has nodal points in these locations, thus corresponding with a third-order bending mode. The oscillation at 424 Hz, on the other hand, is interpreted as a first-order bending mode.

A further spectrogram (see Fig. 14, right) displays the variations of the frequency contributions along the span of the plate (for  $x/a = 0.5$ ). This reveals a very good spanwise homogeneity, with the different frequency contributions having little or no variations along the entire span, which is consistent with a quasi-2D panel vibration.

### 3.4 Phase-average description

To quantitatively describe the behavior of the flow and the structure in the different stages of the shock induced panel flutter cycle, a phase averaging of the displacement and velocity data has been carried out. Four phases have been defined according to the value and the rate-of-change of the panel displacement at the center ( $x/a = 0.5$  and  $y/a = 0$ ).

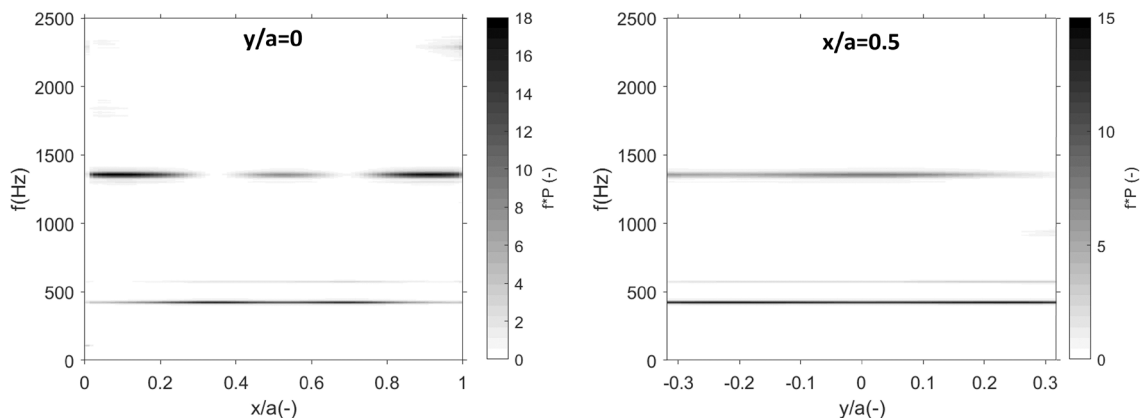


Fig. 14 Spectrogram along chord (left) and span (right) of the panel

Phase 1 and 3 include, respectively, all the snapshots in which the largest positive and negative deformation of the panel are experienced. Phase 2 and 4 are two intermediate phases, in which the displacement of the panel is, respectively, decreasing and increasing.

With the phase averaging procedure, the displacement is described as:  $z = z_{avg} + z_{per} + z_{fluct}$ , where  $z_{avg}$  is the average displacement,  $z_{per}$  the periodic contribution and  $z_{fluct}$  the remaining fluctuating (random) component. In Fig. 15, the phase average displacement ( $z_{phs}$ ) is given, which is defined as the sum  $z_{phs} = z_{per} + z_{avg}$ .

First of all it is worth noticing that also in this representation the distribution of the vertical displacement is found to be remarkably coherent along the span, with small deviations present only toward the edges of the panel.

In the top left image the average displacement in the first flutter phase is visualized where, as anticipated, the panel has the largest positive displacement, reaching a maximum value of  $z_{phs}/h \approx 4$  at  $x/a = 0.25$ . Relatively small negative displacements are observed in the second downstream half of the panel.

In the following flutter phase, the displacement of the first half of the panel is reducing, while it increases in the second half, obtaining an approximately antisymmetric distribution with respect to  $x/a = 0.5$ .

The displacement field of Phase 3 is the opposite of the field of Phase 1, with the largest (negative) displacement  $z_{phs}/h \approx -4$  present in the second half of the panel ( $0.5 < x/a < 1$ ). Continuing the flutter oscillation, in Phase 4 the panel exhibits once again a shape similar to that of Phase 2, with a relatively reduced deformation in the whole panel area, similar to the average displacement shown in Fig. 9.

The same phase averaging procedure has been also applied to the simultaneous velocity data using the phase information as extracted from the panel motion, with the phase-averaged velocity field ( $u_{phs}$ ) defined as the sum of the periodic ( $u_{per}$ ) and the average ( $u_{avg}$ ) contributions.

In Fig. 16 the vertical component of the velocity field ( $Vz_{phs}$ ) is displayed, and in Fig. 17 the horizontal component ( $Vx_{phs}$ ). The vertical velocity component is particularly efficient in showing variations in the shock position

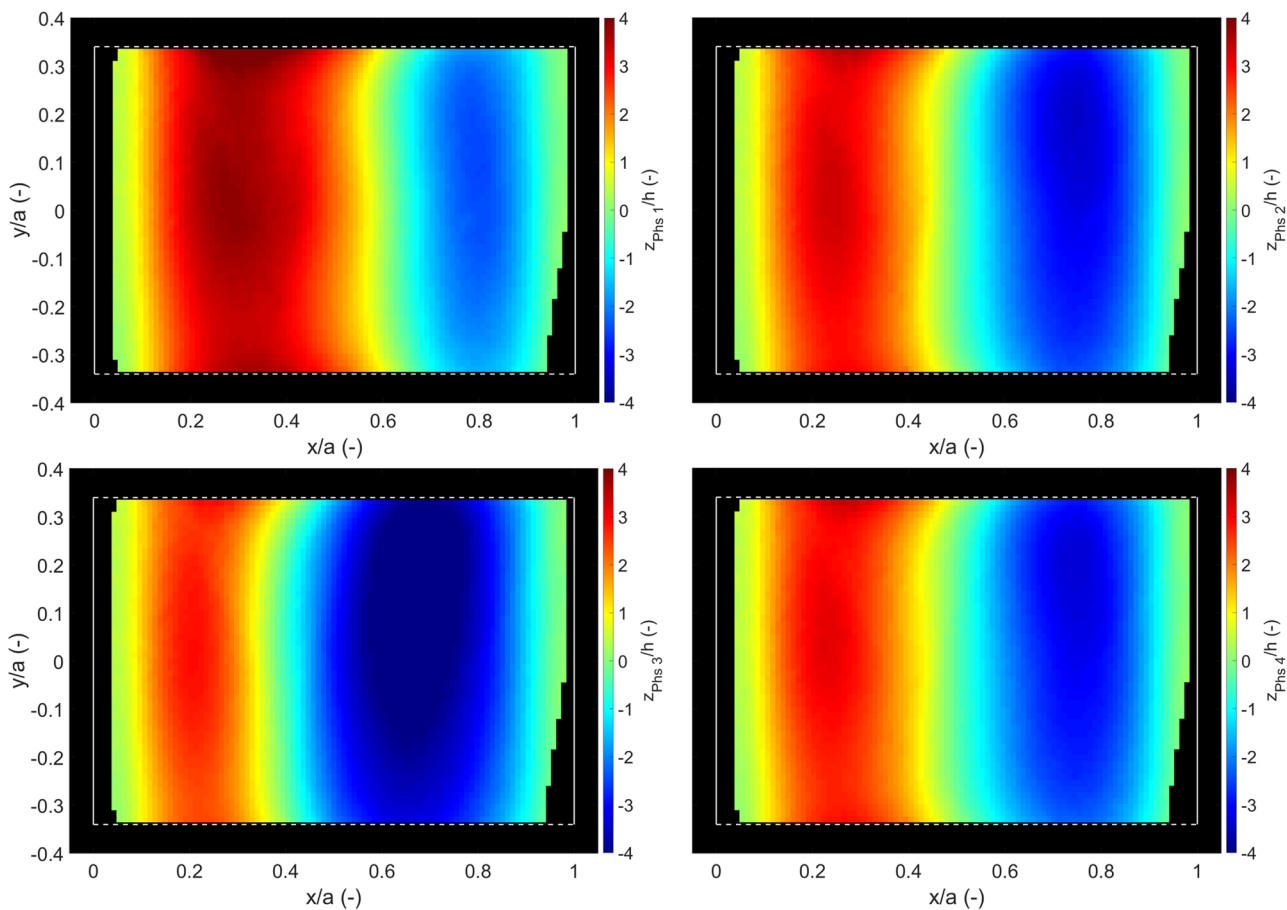


**Fig. 15** DIC phase averaged displacement field ( $z/h$ ). Phase 1 and 2 on the top left and right, respectively, while Phase 3 and 4 on the bottom left and right

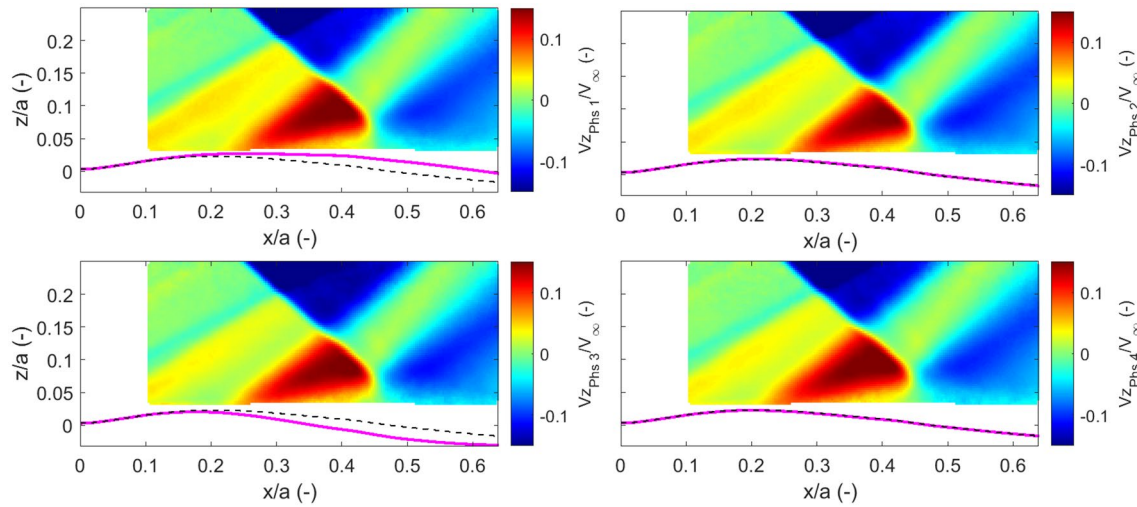


**Fig. 16** PIV phase averaged vertical velocity field ( $V_z/V_\infty$ ). Phase 1 and 2 on the top left and right, respectively, Phase 3 and 4 on the bottom left and right. On the bottom, the respective phase-averaged panel displacement fields (magenta lines) are compared to the aver-

age panel displacement field (dashed black line) for  $y/a = 0$ . Panel displacement is pre-multiplied by a factor of three to facilitate visualization

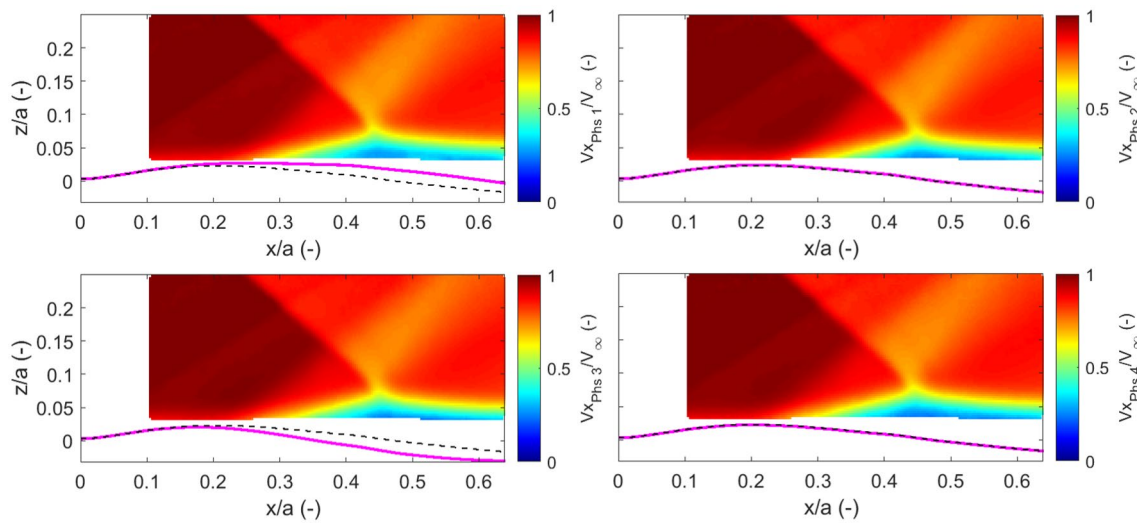


**Fig. 17** PIV phase averaged horizontal velocity field ( $V_x/V_\infty$ ). Phase 1 and 2 on the top left and right, respectively, Phase 3 and 4 on the bottom left and right. On the bottom, the respective phase-averaged panel displacement fields (magenta lines) are compared to the aver-

age panel displacement field (dashed black line) for  $y/a = 0$ . Panel displacement is pre-multiplied by a factor of three to facilitate visualization

and in the intensity of pressure waves in the front of the panel, while the horizontal component allows to better visualize variations in the extent of the separated area. Together with the phase averaged velocity fields, the profiles of the phase-averaged displacement in the panel centerline ( $y/a = 0$ ) are shown in the bottom of both Figs. 16 and 17. These profiles (magenta lines) are compared to the profile of the average displacement field (black dashed

line) and to better illustrate the panel movement, the panel deflections are multiplied by a factor of three.

Although the plate displays an upwards deflection at the leading edge in all phases, a variation in the strength of the compression waves in the front region of the panel ( $0 < x/a < 0.2$ ) is observed among the different phases. In detail, the compression is the strongest in Phase 1, in which the front of the panel experiences the largest deformation.

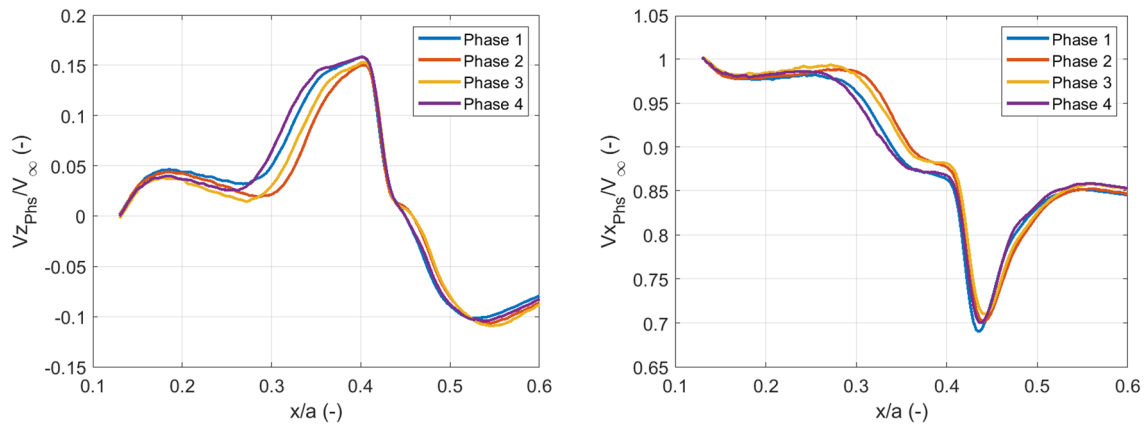


**Fig. 18** Profile of phase-averaged velocity fields for  $z/a = 0.1$  for  $V_z$  (left) and  $V_x$  (right)

This information is clarified in Fig. 18, which shows the profile of  $V_{z_{phs}}$  and  $V_{x_{phs}}$  for all the flutter phases and for  $z/a = 0.1$ . These velocity profiles also confirm that in Phase 1 the reflected shockwave is half-way between its most upstream and downstream position.

In the following phase, the displacement in the first half of the panel is reduced and as a consequence also the strength of the front compression waves. In this phase the reflected shockwave is in its most downstream location (see Figs. 16 and 18) and therefore the interaction length and the separated area size are reduced as well, as can be seen from the figures showing the horizontal velocity component (Fig. 17).

In Phase 3 the panel experiences the most downward deflection when compared to the mean displacement, thus the compression waves at the front of the panel are the weakest. Furthermore, the shockwave is in its upstream travel.

During Phase 4 the shockwave has reached its most upstream position, therefore, the largest interaction length and an increased separated area are observed, while the front compression waves have once again intensified in strength. As a result of the different interactions in the four flutter phases, the velocity profiles in Fig. 18 suggest that for Phase 1 and Phase 4 the expansion waves originating downstream of the impinging shockwave are more intense.

It is interesting to note that, although Phase 2 and 4 are very similar in terms of panel displacement, this does not apply for the flow field, where the combination of pressure waves, separated area and shockwave position is different for each flutter phase.

### 3.5 Proper orthogonal decomposition

A modal analysis of the structure displacement has been determined from a POD computation. The snapshot POD method has been applied to the panel displacement field,

extracting a spatio-temporal decomposition, of the fluctuating part of the displacement signal:

$$z(\vec{x}, t) = z_{avg}(\vec{x}) + z'(\vec{x}, t) = z_{avg}(\vec{x}) + \sum_{j=1}^N \sqrt{\lambda_j} \cdot a_j(t) \cdot \vec{\phi}_j(\vec{x}) \tag{1}$$

Here,  $a_j(t)$  and  $\vec{\phi}_j(\vec{x})$  are, respectively, the orthonormal time coefficients and the orthogonal spatial POD functions, while  $N$  is the total number of modes which is equal to the number of snapshots ( $N=4719$ ).  $\lambda_j$  are the POD eigenvalues of the problem from which the energy contribution associated with each POD mode is evaluated.

The relative energy fraction given by the ratio  $\lambda_i / \sum \lambda$  is shown in Fig. 19 for the first 10 modes, showing that the first mode accounts for 77% of the total energy, while the sum of the first two modes is equal to 92%. From the third mode on the energy contribution is lower than 2% per mode. This suggests that the flutter dynamics is dominated by the first two modes and for this reason, in the following discussion only the first and the second modes will be further analyzed.

From the eigenvalues and the orthogonal spatial functions, the spatial modes are obtained as:

$$z_{mode}(j) = \sqrt{\lambda(j)} \cdot \vec{\phi}_j(\vec{x}) \tag{2}$$

The first spatial mode (see Fig. 20) has a typical first bending mode shape, with main variation at central streamwise locations. The behavior is very coherent along the span, with minor spanwise variations being present only in proximity of the free edges of the panel.

The first mode shape is very similar to the standard deviation of the plate displacement, shown in Fig. 9, which is not surprising in view of the high relative energy content of this mode. However, some differences can be observed. In the standard deviation plot, the larger values of fluctuations are

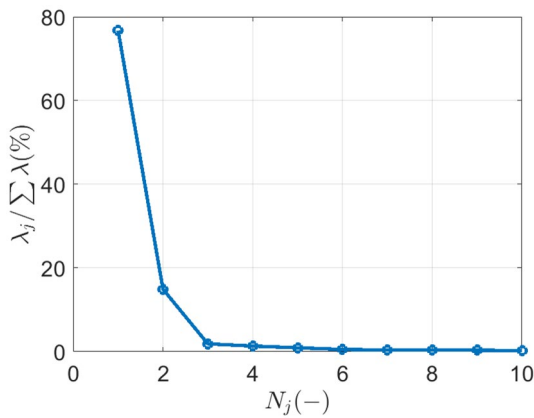


Fig. 19 Energy fraction per eigenvalue

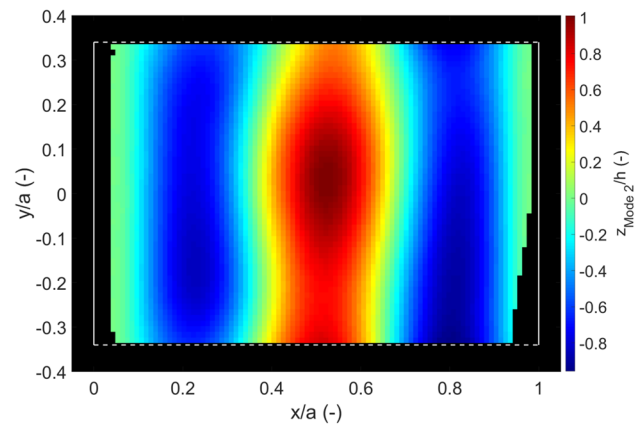


Fig. 21 Second structural POD mode

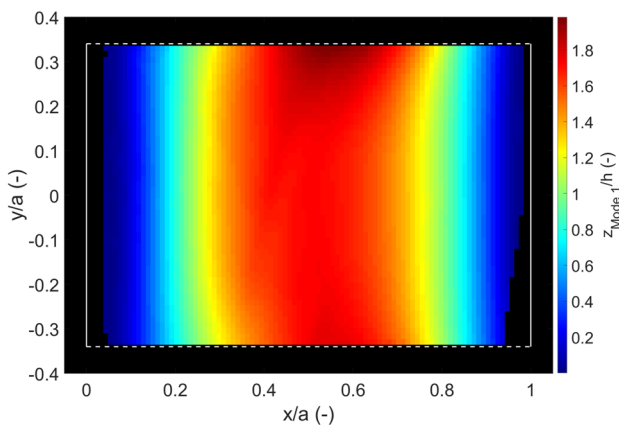


Fig. 20 First structural POD mode

restricted to a very small band which goes from  $x/c = 0.45$  to  $x/c = 0.55$ , while the first mode basically has a high plateau between  $x/c = 0.35$  and  $x/c = 0.65$ . These differences are ascribed to the contributions of the higher order modes.

The second POD mode has a typical third bending mode shape with three distinct regions, with the center region of oscillations being of opposite sign with respect to the other two (see Fig. 21). For this mode too, only marginal spanwise discrepancies are observable.

In Shinde et al. (2021) snapshot-POD has been applied to the study of the structural modes of a thin panel that is clamped on all sides with an aspect ratio  $a/b=0.73$ . That paper demonstrated that most of the dynamic energy of the panel is associated with the first two POD modes, and as such in good agreement with the current study (see Fig. 19). In Shinde et al. (2021) the first two modes having, respectively, a first and a third bending mode shape, with the former being the dominant mode also in the operational modal analysis computed by Spottswood et al. (2012) for a similar panel with  $a/b=2$ . These two mode shapes (for a fully

clamped panel) can be considered analogous of the first two modes obtained in the current study for a panel with two free sides.

To appreciate the periodicity of the first two modes, the autocorrelations of the corresponding time coefficients have been computed (see Fig. 22, left). Both signals appear as very periodic with the second mode (green line) displaying a frequency approximately three times that of the first POD mode (red line). This observation is confirmed by the PSD of the time coefficients (see Fig. 22, right). The first mode has a main contribution at 424 Hz and a small contribution at 576 Hz. On the other hand the PSD of the second time coefficient has only one peak at 1354 Hz. These frequency peaks are indeed the same as those observed in Fig. 13 for the spectral content of the panel movement and of the reflected shock-wave position. This observation further justifies the use of the first two structural modes as being sufficient for describing the oscillation of the panel. Also, the spatio-temporal behavior of the two identified POD modes is in direct agreement with the structural dynamic behavior as identified from the spectrograms in Fig. 14.

### 3.6 Separated area analysis

A main aspect of shock induced panel flutter is the dynamics of the separated area in the interaction region. Before analyzing the interaction between the panel oscillation and the pulsation of the separated area (and the other flow features), the SWBLI is here discussed separately, by comparing the separated area developing above the thin and the rigid panel.

The comparison of the two average horizontal velocity fields in Fig. 10 confirms an increase in the average separated area size for the thin flexible panel. This is also corroborated by the position of the average reflected shockwave position, which for the thin panel is located at  $X_{SW} = 0.24a$  ( $X_{SW} = 5.91\delta_{99,0}$ ), while for the rigid panel at  $X_{SW} = 0.27a$



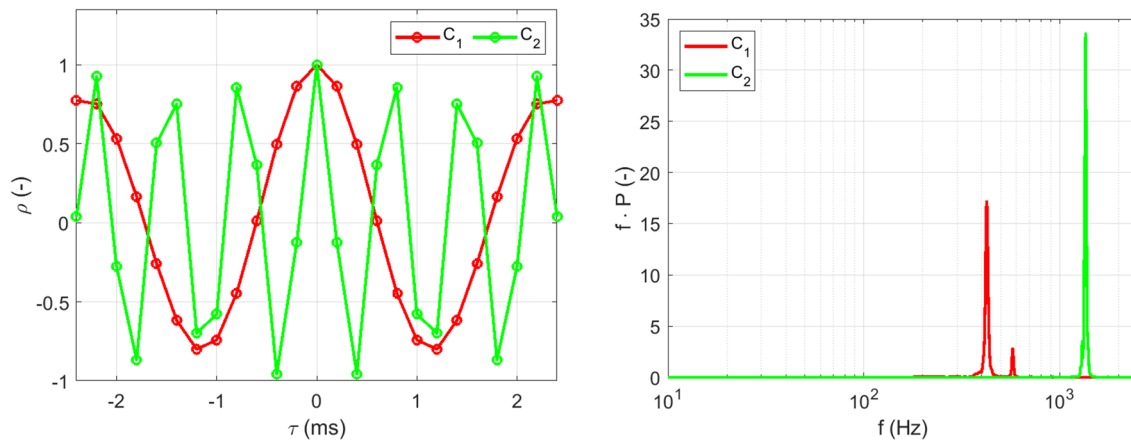


Fig. 22 Autocorrelation of time coefficients (left) and relative spectrum (right)

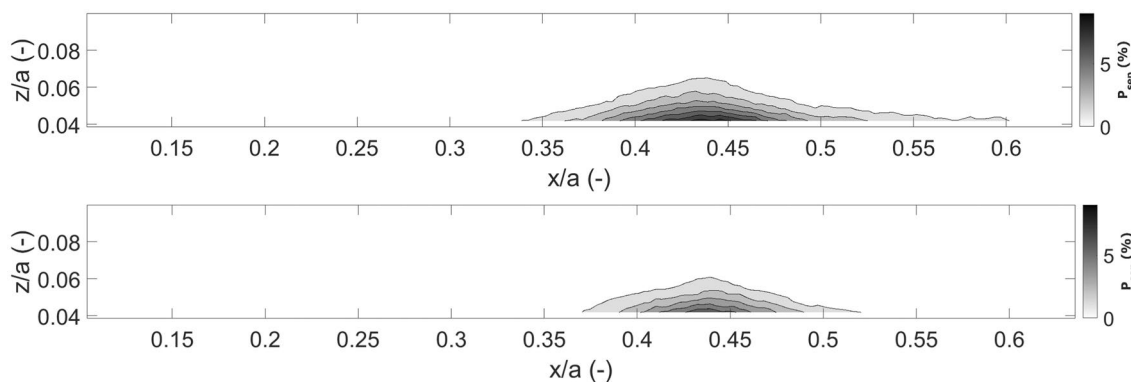


Fig. 23 Probability of separated area for flexible (top) and rigid (bottom) panel

( $X_{SW} = 6.65\delta_{99,0}$ ). Since the position of the impinging shockwave is fixed, this implies that the interaction length has increased for the flexible panel. The interaction length has been quantified with the same approach as in Dussauge et al. (2006) and Pasquariello et al. (2015) and defined as the distance between the extrapolated impingement points of both the median reflected and impinging shockwaves (see Fig. 1, left). The results show that for the flexible panel there is an increase in the interaction length ( $L_{int}$ ) of 8%, see Table.5. Such an increase in  $L_{int}$  is in agreement with the qualitative observation present in the experimental study of Daub et al. (2016b), but it is in contradiction with the numerical findings of Pasquariello et al. (2015), where a reduction in interaction length was observed for the flexible panel. However, in these studies different shock-impingement positions and strengths were considered, which may affect the outcome.

To quantitatively analyze the extent of the separated area, the probability of separation ( $P_{sep}$ ) has been computed at each location, as the percentage of vectors with negative streamwise velocity, using the same approach as described

Table 5 SWBLI parameters

Panel	Flexible	Rigid
$STD(X_{SW})/\delta_{99,0}(-)$	0.65	0.36
$L_{int}/\delta_{99,0}(-)$	8.73	8.06
$A_{sep}/\delta_{99,0}^2(-)$	5.64	3.28

by Giepmans et al. (2018). The results are plotted in Fig. 23 for  $0.038 < z/a < 0.11$  and clearly exhibit that, in presence of the flexible panel (top), the region where reverse flow may occur is much larger. By spatially integrating the probability of separation, the average separation area ( $A_{sep}$ ) is obtained as an overall metric of the separation extent, confirming the increase in the separated area for the flexible panel, as summarized in Table 5.

The observed increase in the separated area size is again in good agreement with Daub et al. (2016b), while being in contradiction with the numerical study of Visbal (2014) who proposed that a flexible panel could be used as a passive flow control device to reduce the extent of the separated region.

Therefore, in light of the current findings and those in literature, it remains uncertain what the effect of a flexible surface on the separation extent is, and which structural parameters have an influence.

### 3.7 Fluid-structure correlation

From the phase average analysis in Figs. 16, 17 it has been observed that the reflected shockwave reaches its most upstream/downstream position in a different phase with respect to the most upward/downward deflection of the panel. This phase delay is verified by the cross-correlation between the dimensionalized reflected shockwave position ( $\bar{x}_{SW} = X_{SW}/a$ ) and the panel vertical displacement ( $\bar{z} = z/h$ ) which is shown in Fig. 24.  $\bar{z}$  has been considered in a point of the panel in the center of the range of oscillation of the reflected shockwave, thus in  $x/a = 0.25, y/a = 0$ . The plot reveals that the maximum correlation is obtained for a lag  $\tau = 0.6\text{ ms}$ , which is equal to one quarter of the flutter cycle, confirming what was observed qualitatively in Fig. 12. The periodical behavior of the cross-correlation corroborates the presence of a strong coupling between the panel movement and the reflected shockwave position and therefore an exchange of energy between the flow and the structure, in

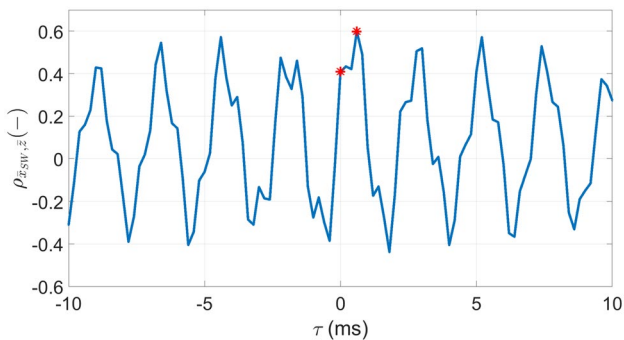


**Fig. 24** Cross-correlation between reflected shockwave and displacement of the structure in  $x/a = 0.25$  and  $y/a = 0$ . '\*' indicates the values of  $\tau$  for which the correlation maps are later shown

view of the phase shift of 90 degrees between structural and shock motion.

The coupling between flow and structure not only concerns the reflected shockwave movement, but also the interaction region as a whole. To better characterize this aspect, a cross-correlation between all the points of the velocity field and the same panel point ( $x/a = 0.25, y/a = 0$ ) has been carried out. The results are shown in the form of a correlation map, showing at each point in the velocity field, the correlation value for zero time lag  $\rho(\tau = 0\text{ms})$ , for both velocity components (see Fig. 25).

The cross-correlation map indicates that there is a high degree of correlation ( $|\rho| \approx 0.75$ ) between the panel displacement at  $x/a = 0.25$  and the velocity field in the region between the leading edge compression wave and the reflected shockwave  $0 < x/a < 0.2$ . These high correlation values can be explained by the fact that for a positive (upward) displacement of the panel, compression waves at the front of the panel increase in strength, hereby decreasing the streamwise and increasing the wall normal velocity components, resulting in negative and positive correlation values, respectively. On the other hand, a significant but lower correlation value ( $|\rho| \approx 0.3$ ) is observable in the shock oscillation range.

Inspired by the results of Fig. 24, the correlation maps are also determined (Fig. 26) for a time delay of 0.6 ms ( $\rho(\tau = 0.6\text{ms})$ ), revealing a relatively high correlation ( $|\rho| \approx 0.6$ ) in the reflected shockwave oscillation range. The sign of the correlation is once again opposite for the two velocity components, since for more upstream shockwave positions there is an earlier (in terms of streamwise positions) decrease in the horizontal component of velocity and an earlier upward deflection of the streamlines.

For the horizontal velocity component (Fig. 26, left), the regions of positive correlation are seen to extend to the entire interaction length and separated area, confirming the link between the reflected shockwave position and the separated area. For the vertical velocity component (Fig. 26, right), downstream of the shockwave oscillation range, there is a further positive correlation area. This region is associated with the dynamics of the expansion waves originating from

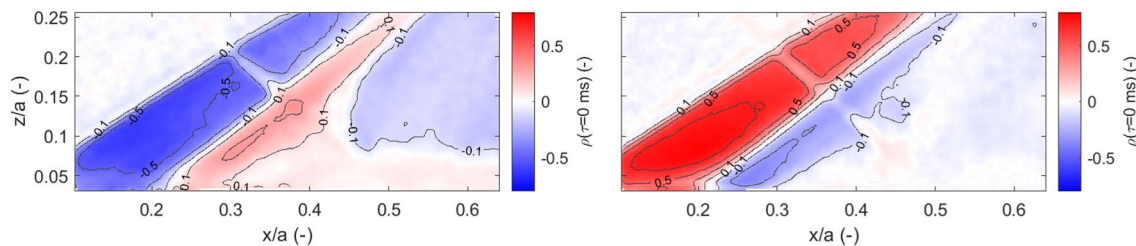


**Fig. 25** Cross-correlation between flow field (on the left  $V_x$  and on the right  $V_z$ ) and displacement of the structure ( $z/h$ ) in  $x/a = 0.25$  and  $y/a = 0$  for  $\tau=0\text{ ms}$

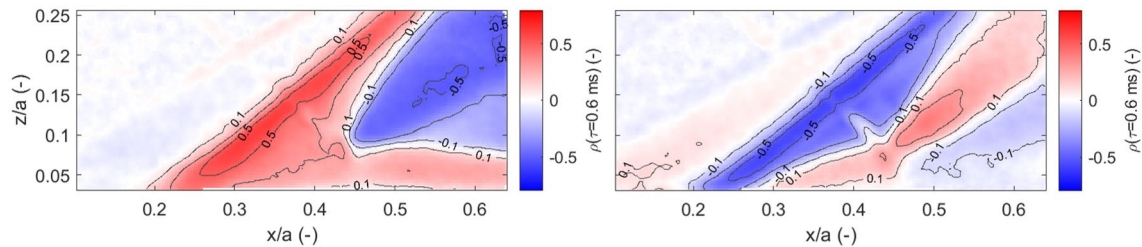


**Fig. 26** Cross-correlation between flow field (on the left  $V_x$  and on the right  $V_z$ ) and displacement of the structure ( $z/h$ ) in  $x/a=0.25$  and  $y/a=0$  for  $\tau=0.6$  ms

the interaction between the sonic line and the impinging shockwave, as sketched in Fig. 1 (left). For the  $V_x$  correlation map, for  $x/a > 0.45$  and  $z/a > 0.1$  a region of high negative correlation is present in that area, suggesting that for more downstream locations of the reflected shockwave, the horizontal component of velocity is lower.

Upstream of the reflected shockwave ( $x/a < 0.2$ ) no relevant correlation between the panel and the flow is observed neither for the horizontal nor for the vertical component of velocity. This result was expected since the flow in this region is governed by the instantaneous local shape of the panel, which is out of phase with the reference displacement point for the considered time delay.

## 4 Discussion and conclusions

The reported findings show that an experimental simultaneous and time-resolved full-field analysis of structure and flow for shock induced panel flutter is feasible with the proposed techniques. This was the first investigation in which DIC and PIV have been employed in combination for studying this phenomenon, confirming the results obtained by Hortensius et al. (2018) for a similar application (although in this study neither the flow nor the structure were time resolved).

In this study a good quality of the experimental data was achieved by optically separating the structure and flow measurements. The use of fluorescent paint, a dedicated blue LED illumination source and DIC highpass filters managed to noticeably reduce the interference of the PIV system on the DIC acquisitions. On the other hand, the use of a PIV bandpass filter helped to minimize interference from the DIC measurement system, however this was found not to be very critical. Given the results obtained, this set-up was demonstrated to be suitable for a simultaneous PIV and DIC measurements.

The DIC measurements confirm the spanwise coherence of the (static and dynamic) displacement field (Fig. 9) as anticipated from the applied boundary conditions with free panel edges. This also justifies the use of planar PIV

measurements in the centerline of the panel to characterize the flow. In applications where 3D structures are expected (like for the study of a panel clamped on all the four edges), however, a more elaborate (multiple-plane or volumetric) PIV approach may be required to properly characterize the flow field.

The DIC data show that the mean displacement has the shape of a second bending mode, with an upwards deflection at the front and a downwards deflection at the rear. This agrees with the expected variation of the pressure over the panel, which increases in downstream direction due to the impinging shockwave. As the average value of the panel displacement is approximately zero, this suggests that the cavity pressure is approximately equal to the mean pressure over the panel, as a result of the ventilation effect of both the side slits in the panel as well as the open end of the cavity itself.

The oscillation amplitude of the panel is well beyond the commonly accepted flutter limit, with an amplitude  $\Delta z/h \approx 8$  (Fig. 12). The oscillation dynamics are dominated by two modes; the strongest is a first bending mode occurring at 424 Hz, and the second a third order bending mode at 1354 Hz, which account for 77% and 15% of the vibration energy, respectively. The interconnection between the flow and the structure is illustrated by a similar spectral content of the displacement of the panel and of the reflected shockwave position, with the latter having a phase lag of approximately a quarter of the flutter cycle (Figs. 12 and 16 - 17). The Strouhal number corresponding to the main contribution (first flutter mode) of the shockwave oscillations (based on the mean interaction length) amounts to  $St = 0.044$  and appears slightly shifted to higher  $St$  when compared to the values of the most relevant contributions ( $St = 0.019 - 0.033$ ) obtained for a rigid panel (see van Oudheusden et al. 2011).

Apart from the general observation of the phase lag of the reflected shock with respect to the panel motion referred to above, a more detailed cross-correlation between the panel movement and the complete flow field was performed. This showed that the region of the flow included between the leading edge compression wave and the reflected shockwave is directly in phase with the panel

oscillation (Fig. 25). In contrast, the velocity fluctuations in proximity to the reflected shockwave have a delay of 0.6 ms with respect to the panel motion (Fig. 26). This lag is also observed in the phase average analysis, in terms of a quarter cycle delay between the reflected shockwave signal and the panel displacement.

The panel and the shockwave movement are the result of a fluid structure interaction, and it is not straightforward to directly establish a cause-consequence relationship between the flow and the structural behavior. Nevertheless some observations can be made to assist the understanding of the shockwave behavior in response to the panel deformation by comparing the performance of the flexible and the rigid panels. First of all the reflected shockwave motion locks on the structural vibration modes of the panel. When comparing the spectra of the reflected shockwave position for the flexible and the rigid panels (Fig. 13), it is evident that the low-frequencies ( $f < 350$  Hz) are not affected. At higher frequencies the flow is clearly energized by the panel oscillation. Thus, it is likely that the low frequency unsteadiness of the SWBLI which is described by the model by Piponniau et al. (2009) for a rigid surface, is still present for the flexible panel, but playing a less relevant role in view of the more energetic contributions at higher frequencies. In a recent investigation of a fluid-structure interaction in hypersonic flow, Daub et al. (2022) too, recognized that the role of intrinsic SWBLI unsteadiness on the panel dynamics remains unclear. Although additional research is required, another aspect which could influence the SWBLI dynamics for the flexible panel is the presence of compression waves at the front of the panel, which variation in strength is associated with the local slope of the panel and hence changing with the frequency of oscillation of the structure.

As a result of the more dynamic interaction, the standard deviation of the reflected shockwave position increases by approximately 80% for the flexible panel and a similar increase ( $\approx 70\%$ ) is also observed for the extent of the separated area (see Table 5). This trend is in agreement with the experimental results of Daub et al. (2016a) but in disagreement with the numerical studies of Pasquariello et al. (2015) and Visbal (2014). This discrepancy suggests that either the separated area extent is very sensitive to the simulation parameters, or that particular conditions which may be present in the experiments, such as a different cavity pressure, could affect the SWBLI under such conditions. Thus, in future studies it is recommended to measure and vary the cavity pressure.

As such, the obtained data allow to scrutinize the flow and structural dynamics in their interaction and in this way can further contribute to the clarification of the phenomenon of shock-induced flutter.

**Acknowledgements** The authors acknowledge LaVison for having provided two LED lights for the experiments conducted in this study.

**Author Contributions** All authors contributed to the study conception, design and preparation. Data collection and analysis were performed by AD and PQA. The first draft of the manuscript was written by AD, FS and BvO commented on previous versions of the manuscript. All authors read and approved the final manuscript.

**Funding** This work has been carried out as part of the project HOMER (Holistic Optical Metrology for Aero-Elastic Research), funded by the European Commission, program H2020 under Grant No. 769237.

**Availability of data and materials** Data and materials that support the findings of this study are available on request from the corresponding author.

## Declarations

**Ethical approval** Not applicable.

**Competing interests** The authors declare they have no conflict of interest.

**Open Access** This article is licensed under a Creative Commons Attribution 4.0 International License, which permits use, sharing, adaptation, distribution and reproduction in any medium or format, as long as you give appropriate credit to the original author(s) and the source, provide a link to the Creative Commons licence, and indicate if changes were made. The images or other third party material in this article are included in the article's Creative Commons licence, unless indicated otherwise in a credit line to the material. If material is not included in the article's Creative Commons licence and your intended use is not permitted by statutory regulation or exceeds the permitted use, you will need to obtain permission directly from the copyright holder. To view a copy of this licence, visit <http://creativecommons.org/licenses/by/4.0/>.

## References

- Ahn YJ, Eitner MA, Musta MN, Sirohi J, Clemens NT, Rafati S (2022) Experimental investigation of flow-structure interaction for a compliant panel under a Mach 2 compression-ramp. in AIAA Scitech 2022 Forum. AIAA 2022-0293
- Anderson W (1962) Experiments on the flutter of flat and slightly curved panels at mach number 2.81. Technical report. California Institute of Technology and United States
- Babinsky H, Harvey J (2011) Shock Wave-Boundary-Layer Interactions. Cambridge University Press, Cambridge Aerospace Series
- Beberrnis T, Spottswood S, and Eason T (2011) High-speed digital image correlation measurements of random nonlinear dynamic response. in Proulx, T. (eds) Experimental and Applied Mechanics, Vol 6. Conference Proceedings of the Society for Experimental Mechanics Series. vol 6. pp 171–186
- Beberrnis TJ, Ehrhardt D (2021) Visible light refraction effects on high-speed stereo digital image correlation measurement of a thin panel in Mach 2 flow. Exp Tech 45:241–255
- Beberrnis TJ, Spottswood SM, Perez RA, Eason TG (2016) Nonlinear response of a thin panel in a multidiscipline environment: part i-experimental results. in Kerschen, G. (eds) Nonlinear Dynamics. Conference Proceedings of the Society for Experimental Mechanics Series. vol 1. pp 237–248
- Beresh S, Comninou M, Clemens N, Dolling D (1998) The effects of the incoming turbulent boundary layer structure on a

- shock-induced separated flow. in 36th AIAA Aerospace Sciences Meeting and Exhibit. AIAA 1998-620. Reno, USA
- Bermejo-Moreno I, Campo L, Larsson J, Bodart J, Helmer D, Eaton J (2014) Confinement effects in shock wave/turbulent boundary layer interactions through wall-modelled large-eddy simulations. *J Fluid Mech* 758:5–62
- Blevins RD, Holehouse I, Wentz KR (1993) Thermoacoustic loads and fatigue of hypersonic vehicle skin panels. *J Aircr* 30:971–978
- Boyer N, McNamara J, Gaitonde D, Barnes C, Visbal M (2018) Features of shock-induced panel flutter in three-dimensional inviscid flow. *J Fluids Struct* 83:490–506
- Boyer NR, McNamara J, Gaitonde D, Barnes CJ, Visbal MR (2021) Features of panel flutter response to shock boundary layer interactions. *J Fluids Struct* 101:103207
- Brouwer KR, Gogulapati A, McNamara JJ (2017) Interplay of surface deformation and shock-induced separation in shock/boundary-layer interactions. *AIAA J* 55:4258–4273
- Brouwer KR, Perez R, Bebernis TJ, Spottswood SM, Ehrhardt DA (2021) Fluid-structure interaction on a thin panel including shock impingement effects. in AIAA Scitech 2021 Forum. AIAA 2021-0910
- Clemens NT, Narayanaswamy V (2014) Low-frequency unsteadiness of shock wave/turbulent boundary layer interactions. *Annu Rev Fluid Mech* 46:469–492
- D'Aguanno A, Mathijssen LCJM, Schrijer FFJ, van Oudheusden BW (2019) Experimental investigation of supersonic panel flutter. in International Conference on Flight vehicles, Aerothermodynamics and Re-entry Missions and Engineering (FAR 2019). Monopoli, Italy
- Daub D, Esser B, Gülhan A (2020) Experiments on high-temperature hypersonic fluid-structure interaction with plastic deformation. *AIAA J* 58:1423–1431
- Daub D, Willems S, Gülhan A (2016) Experimental results on unsteady shock-wave/boundary-layer interaction induced by an impinging shock. *CEAS Space J* 8:3–12
- Daub D, Willems S, Gülhan A (2016) Experiments on the interaction of a fast-moving shock with an elastic panel. *AIAA J* 54:670–678
- Daub D, Willems S, Gülhan A (2022) Experiments on aeroelastically fluid-structure interaction in hypersonic flow. *J Sound Vib* 531:116714
- Dolling DS (2001) Fifty years of shock-wave/boundary-layer interaction research: what next? *AIAA J* 39:1517–1531
- Dowell EH (1970) Panel flutter - a review of the aeroelastic stability of plates and shells. *AIAA J* 8:385–399
- Dowell EH (1975) Aeroelasticity of plates and shells. Noordhoff International Pub Leiden
- Dowell EH, Bendiksen O (2010) Panel Flutter. pp 1–14. *Encyclopedia of Aerospace Engineering*
- Dowell EH, Voss HM (1965) Theoretical and experimental panel flutter studies in the mach number range 1.0 to 5.0. *AIAA J* 3:2292–2304
- Dupont P, Haddad C, Debiève JF (2006) Space and time organization in a shock-induced separated boundary layer. *J Fluid Mech* 559:255–277
- Dussauge JP, Dupont P, Debiève JF (2006) Unsteadiness in shock wave boundary layer interactions with separation. *Aerosp Sci Technol* 10:85–91
- Ganapathisubramani B, Clemens NT, Dolling DS (2009) Low-frequency dynamics of shock-induced separation in a compression ramp interaction. *J Fluid Mech* 636:397–425
- Garelli L, Paz R, Storti M (2010) Fluid-structure interaction study of the start-up of a rocket engine nozzle. *Comput Fluids* 39:1208–1218
- Giepmans RHM, Schrijer FFJ, van Oudheusden BW (2018) A parametric study of laminar and transitional oblique shock wave reflections. *J Fluid Mech* 844:187–215
- Hortensius R, Dutton JC, Elliott GS (2018) Simultaneous flowfield and surface-deflection measurements of an axisymmetric jet and adjacent surface. *AIAA J* 56:917–932
- Humble R, Scarano F, Oudheusden BW (2007) Particle image velocimetry measurements of a shock wave/turbulent boundary layer interaction. *Exp Fluids* 43:173–183
- Humble RA (2009) Unsteady flow organization of a shock wave/boundary layer interaction. Ph.D. thesis. Delft University of Technology. ISBN: 978-90-597-2295-8
- Humble RA, Elsinga GE, Scarano F, van Oudheusden BW (2009) Three-dimensional instantaneous structure of a shock wave/turbulent boundary layer interaction. *J Fluid Mech* 622:33–62
- Mei C, Abdel-Motagaly K, Chen R (1999) Review of nonlinear panel flutter at supersonic and hypersonic speeds. *Appl Mech Rev* 52:321–332
- Neet MC and Austin JM (2020) Effects of surface compliance on shock boundary layer interaction in the Caltech Mach 4 Ludwig Tube. in AIAA Scitech 2020 Forum. AIAA 2020-0816. Orlando, USA
- Östlund J, Damgaard T, Frey M (2004) Side-load phenomena in highly overexpanded rocket nozzles. *J Propuls Power* 20:695–704
- Pasquariello V (2018) Analysis and control of shock-wave / turbulent boundary-layer interactions on rigid and flexible walls. Ph.D. thesis. Technische Universität München
- Pasquariello V, Hickel S, Adams N, Hammerl G, Wall W, Daub D, Willems S, Gülhan A (2015) Coupled simulation of shock-wave/turbulent boundary-layer interaction over a flexible panel. in 6th European Conference for Aerospace Sciences. number 451 in Conference Proceedings online. pp 1–15. Krakow, Poland
- Piponnier S, Dussauge JP, Debiève JF, Dupont P (2009) A simple model for low-frequency unsteadiness in shock-induced separation. *J Fluid Mech* 629:87–108
- Ragni D, Schrijer FFJ, van Oudheusden BW, Scarano F (2011) Particle tracer response across shocks measured by PIV. *Exp Fluids* 50:53–64
- Schreyer AM, Lasserre JJ, Dupont P (2015) Development of a dual-PIV system for high-speed flow applications. *Exp Fluids* 56(10):1–12
- Sciacchitano A, Scarano F (2014) Elimination of PIV light reflections via a temporal high pass filter. *Meas Sci Technol* 25:084009
- Shinde V, McNamara J, Gaitonde D, Barnes C, Visbal M (2018) Panel flutter induced by transitional shock wave boundary layer interaction. in 2018 Fluid Dynamics Conference. AIAA 2018-3548. Atlanta, USA
- Shinde V, McNamara J, Gaitonde D, Barnes C, Visbal M (2019) Transitional shock wave boundary layer interaction over a flexible panel. *J Fluids Struct* 90:263–285
- Shinde VJ, McNamara JJ, Gaitonde DV (2019b) Effect of structural parameters on shock wave boundary layer induced panel flutter. in AIAA Aviation 2019 Forum. AIAA 2019-3716. Dallas, USA
- Shinde VJ, McNamara JJ, Gaitonde DV (2021) Shock wave turbulent boundary layer interaction over a flexible panel. in AIAA Scitech 2021 Forum. AIAA 2021-0488
- Souverein LJ, van Oudheusden BW, Scarano F, Dupont P (2009) Application of a dual-plane particle image velocimetry (Dual-PIV) technique for the unsteadiness characterization of a shock wave turbulent boundary layer interaction. *Meas Sci Technol* 20:074003
- Spottswood SM, Bebernis TJ, Eason TG, Perez RA, Donbar JM, Ehrhardt DA, Riley ZB (2019) Exploring the response of a thin, flexible panel to shock-turbulent boundary-layer interactions. *J Sound Vib* 443:74–89
- Spottswood SM, Eason T, Bebernis T (2012) Influence of Shock-Boundary Layer Interactions on the Dynamic Response of a Flexible Panel. International Conference on Noise and Vibration Engineering (ISMA), vol 2012. Belgium, Leuven, pp 603–616
- Sutton MA, Schreier HW, Orteu J (2009) Image Correlation for Shape, Motion and Deformation Measurements: Basic Concepts. Theory and Applications, Springer, US, New York

- Tripathi A, Gustavsson J, Shoele K, Kumar R (2021) Response of a compliant panel to shock boundary layer interaction at Mach 2. in AIAA Scitech 2021 Forum. AIAA 2021-0489
- van Oudheusden BW, Jöbbsis AJP, Scarano F, Souverein LJ (2011) Investigation of the unsteadiness of a shock-reflection interaction with time-resolved particle image velocimetry. *Shock Waves* 21:397–409
- Visbal M (2012) On the interaction of an oblique shock with a flexible panel. *J Fluids Struct* 30:219–225
- Visbal M (2014) Viscous and inviscid interactions of an oblique shock with a flexible panel. *J Fluids Struct* 48:27–45
- Watts D J (1968) Flight experience with shock impingement and interference heating on the X-15-2 research airplane. NASA TM X-1669
- Whalen TJ, Schöneich AG, Laurence SJ, Sullivan BT, Bodony DJ, Freydin M, Dowell EH, Buck GM (2020) Hypersonic fluid-structure interactions in compression corner shock-wave/boundary-layer interaction. *AIAA J* 58:4090–4105
- Willems S, Gülhan A, Esser B (2013) Shock Induced fluid-structure interaction on a flexible wall in supersonic turbulent flow. in Array, editor. *EUCASS Proc Ser - Adv AeroSp Sci* 5:285–308
- Zhang P, Porfiri M (2019) A combined digital image correlation/particle image velocimetry study of water-backed impact. *Comp Struct* 224:111010

**Publisher's Note** Springer Nature remains neutral with regard to jurisdictional claims in published maps and institutional affiliations.